


Effects of conduction electron excitation on x-ray magnetic circularly polarized emission in itinerant ferromagnets

Akihiro Koide, Takuji Nomura, and Toshiya Inami 

Synchrotron Radiation Research Center, National Institutes for Quantum and Radiological Science and Technology, SPring-8, 1-1-1 Koto, Sayo, Hyogo 679-5148, Japan



(Received 22 July 2020; accepted 29 October 2020; published 22 December 2020)

We develop a theoretical method to calculate x-ray magnetic circularly polarized emission (XMCPE) spectra for itinerant ferromagnets, in particular, $K\alpha$ emission for transition metals. The effects of electron excitations in the d bands are treated by means of the Keldysh Green's function. In our theoretical framework, the ferromagnetic ground state and the excitations are described by a mean-field approximation and a single-bubble diagram, respectively. We apply our method to $K\alpha$ XMCPE spectra of metallic iron, and reproduce the observed tail structures on the low-energy side of each peak. Contributions from the excitations in the d bands depend strongly on the exchange interaction as well as the direct interaction between the $2p$ and $3d$ electrons. The dependence of the spectral intensity on emission angles with respect to the magnetization direction is cosinusoidal, indicating that $K\alpha$ XMCPE can be used to investigate the magnetization directions in bulk ferromagnets.

DOI: [10.1103/PhysRevB.102.224425](https://doi.org/10.1103/PhysRevB.102.224425)

I. INTRODUCTION

Intense and energy-tunable x rays provided by synchrotron radiation have greatly contributed to investigations of magnetic properties in materials. For instance, x-ray magnetic circular dichroism (XMCD) has revealed local magnetic properties around the absorbing atom in various materials over the last three decades [1–5]. XMCD in a magnetized sample is defined as the difference between the absorption coefficients of the right- and left-handed circularly polarized *incident* x rays. The x-ray absorption occurs because of the excitation of a core electron, which makes XMCD element- and orbital-specific, and consequently, XMCD has been widely adopted as a useful probe of magnetic properties.

Instead of observing absorption spectra, the emission spectra can be monitored with the *incident* circular polarization flipped [6–17]. In the first step of emission spectroscopy, incident circularly polarized x rays excite a core electron to an unoccupied state. Subsequently, x rays are emitted when the core hole is relaxed by the other occupied core or valence electron. Therefore, x-ray emission spectra reflect occupied electron states. In particular, when the incident x-ray energy is tuned near an absorption edge, this technique is called magnetic circular dichroism in resonant inelastic x-ray scattering (RIXS-MCD) [8, 10–17]. RIXS-MCD provides detailed information on the relationship between magnetic and orbital states. For example, $2p3d$ RIXS-MCD for $3d$ transition metals (TMs) elucidated which electron orbital contributes to the total magnetic moment by observing dd excitations in hematite [16].

These x-ray emission spectroscopy techniques use *incident* circularly polarized x rays and detect emitted x rays without resolving the polarization of the x-ray emission. Recently, Inami has reported x-ray magnetic circularly polarized

emission (XMCPE) at the $K\alpha$ emission of magnetized metallic iron for the first time [18]. XMCPE is a phenomenon where the *emitted* x rays from a magnetized sample are circularly polarized. In contrast to the emission spectroscopy mentioned above, the incident x rays were not circularly polarized in the reported XMCPE measurement. The flipping ratio of the observed $K\alpha$ XMCPE was substantially larger than that of K-edge XMCD. Furthermore, a large penetration depth can be achieved by using high-energy incident x rays because the energy and polarization of the incident x rays do not affect XMCPE. Therefore, XMCPE is a promising technique for characterizing true bulk magnetism.

In $K\alpha$ XMCPE, a $1s$ electron is excited to a continuum state far from the absorption edges, and the $1s$ core hole is relaxed by a $2p$ electron accompanied by x-ray emission. Since the $1s$ and $2p$ core levels for TM elements are well separated, $K\alpha$ emission spectra are obtained by multiplet calculations, which solve a parameterized multielectron Hamiltonian within a limited orbital space [19]. One of the advantages of the multiplet calculations is the ability to include multielectron excitations which lead to tail or hump structures accompanying main peaks in emission spectra [19]. On the other hand, it is difficult to include the continuum nature reflecting metallic conduction band structure in the multiplet calculations. In another approach, the band structure and the density of states for spin-polarized valence d electrons can be obtained by *ab initio* calculations. *Ab initio* calculations provide not only those fundamental electronic properties but also observed quantities such as XMCD and photoemission spectra of TMs [20–27]. Although *ab initio* calculations can incorporate a real complex band structure, they cannot directly include multielectron excitations because they are based on a one-electron picture such as the density-functional theory. For example, an early calculation of L -edge circularly

polarized x-ray photoemission spectra yielded symmetric spectral peaks, because of the lack of $3d$ electron excitations [27]. Nowadays, there are several techniques which can include multielectron excitations in *ab initio* calculations. Dynamical mean-field theory has been developed to include multielectron excitations caused by $3d$ - $3d$ interactions [28–30]. *Ab initio* calculations based on the Bethe-Salpeter equation can give multiplet terms including the $2p$ - $3d$ interactions [31,32]. However, these calculations have not included the indirectly induced electron excitations accompanying direct transition between core states. We present a theoretical method to calculate $K\alpha$ emission spectra in TMs by Keldysh Green's functions in order to consider the excitations in the d bands accompanying electron transition from $2p$ to $1s$ core states. By using our method, $K\alpha$ XMCPE spectra in metallic iron are theoretically investigated.

This paper presents a theoretical approach for calculating $K\alpha$ XMCPE for itinerant ferromagnets and is organized as follows. In Sec. II A, we discuss a microscopic $K\alpha$ XMCPE process in a magnetic $3d$ TM system. In Sec. II B, the Hamiltonian that describes our system is defined. In Sec. II C, the transition probability from incident to outgoing photons is calculated by a Keldysh diagram and Keldysh Green's functions. In Sec. II D, we calculate the $2p$ Green's function, which describes $2p$ hole transitions accompanied by the excitations in the $3d$ bands. The $2p$ - $3d$ interaction, which splits $2p$ core levels and excites $3d$ electrons, is considered within a mean-field (MF) approximation. Electron excitations in itinerant $3d$ bands are considered within the lowest-order single-bubble approximation, which is equivalent to the first Born approximation. In Sec. III A, the numerical parameters for the calculations are introduced. In Sec. III B, we compare the calculated spectra with experimental data for metallic iron. We also investigate the effects of the electron excitations on $K\alpha$ XMCPE. In Sec. III C, the dependence of the calculated spectra on the direct and exchange interactions between the $2p$ and $3d$ electrons is investigated. In Sec. III D, we show that the dependence of the difference intensity on emission angles with respect to the magnetization direction is cosinusoidal. Section IV provides the conclusion. The MF band Hamiltonian and details of the dipole transition matrix are explained in Appendixes A and B, respectively.

II. THEORETICAL FORMULATION

A. Microscopic processes in $K\alpha$ XMCPE

XMCPE processes involve incident and outgoing photons, the $1s$, $2p$, and $3d$ electrons, and a photoelectron. Figure 1 shows a schematic of a typical process in $K\alpha$ XMCPE including the relative positions among the electron energy levels. The spin-orbit interaction splits the $2p$ levels into $2p_{1/2}$ and $2p_{3/2}$ states. In itinerant magnetic systems, the $3d$ electrons are spin polarized and delocalized to form the spin-dependent broad dispersive bands. The $3d$ spin polarization further splits the $2p_{1/2,3/2}$ levels into sublevels via a local $2p$ - $3d$ interaction. We can regard this effect of the $2p$ - $3d$ interaction on the $2p$ states as an effective field that induces the additional $2p$ sublevel splitting because the spin-orbit interaction among the $2p$ states is sufficiently larger than the $2p$ - $3d$ interaction.

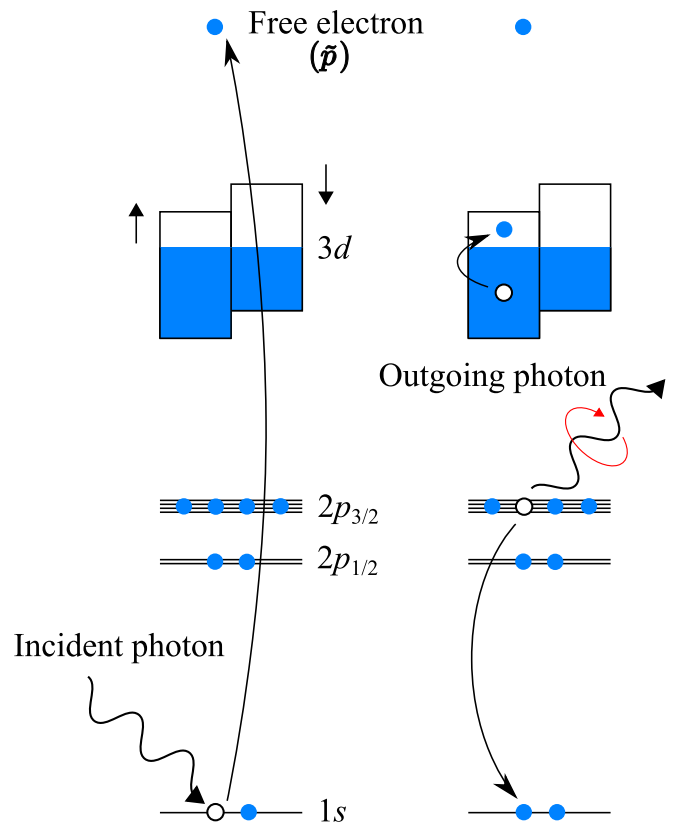


FIG. 1. Schematic of a typical $K\alpha$ XMCPE process. (Left) A $1s$ electron is excited to a free electron state by an incident photon in the first step of $K\alpha$ XMCPE. The free electron states are denoted by \bar{p} . (Right) A circularly polarized photon is emitted by the relaxation of the $1s$ hole by a $2p$ electron. The circular polarization originates from the angular momentum conservation in the $1s$ hole relaxation and the $2p$ hole creation. One of $3d$ conduction electrons can be excited via a $2p$ - $3d$ interaction. The relative positions among the electron energy levels are depicted schematically and are not quantitatively precise.

In the first step of $K\alpha$ XMCPE, the incident x-ray photon kicks out a $1s$ electron to a photoelectron state (left of Fig. 1). We assume that the incident x-ray and photoelectron energies are large enough to recognize the photoelectron as a free electron (denoted by \bar{p} in this paper). Then, the $K\alpha$ XMCPE spectra are independent from the polarization of the incident x rays. This independence from the polarization comes from the follows reasons: The $1s$ hole creation does not depend on the polarization because there is no spin-orbit interaction in the $1s$ states; the free electron has no interaction with the other electrons; and since the $1s$ hole has no orbital angular momentum, the polarization of the emitted x rays in $K\alpha$ XMCPE is determined only by the orbital angular momentum of the $2p$ electron relaxing the $1s$ hole.

After the $1s$ electron excitation, the created $1s$ hole is relaxed by a $2p$ electron and an outgoing photon is emitted (right of Fig. 1). Since each $2p$ sublevel has an orbital angular momentum, the outgoing photon has a circular (or elliptical) polarization to compensate for the $2p$ orbital angular momentum lost by the relaxation to the $1s$ state. In addition, the relaxation process can be accompanied by electron excitations in the $3d$ bands. The $2p$ hole transition within the $2p$ states

in the x-ray emitting atom can occur simultaneously with the 3d electron excitations, although it is not shown explicitly in Fig. 1. We treat the 3d electron excitations within the Born approximation in Sec. II D.

B. Hamiltonian

We focus on a system where a unit cell contains only a 3d TM atom. In this paper all the equations are given in the Hartree atomic units. The total Hamiltonian H consists of the unperturbed Hamiltonian H_0 and the electron-photon interaction H_x :

$$H = H_0 + H_x. \quad (1)$$

H_0 consists of the electron and radiation-field parts:

$$H_0 = H_e + h_r. \quad (2)$$

Before explaining the electron Hamiltonian H_e , we describe H_x and the radiation-field Hamiltonian h_r . h_r is given by

$$h_r = \sum_{\Lambda} \varepsilon_{\Lambda} a_{\Lambda}^{\dagger} a_{\Lambda} \quad (\Lambda \equiv (\mathbf{k}, \lambda)), \quad (3)$$

where \mathbf{k} , and λ are the momentum vector and polarization of a photon, respectively. For simplicity, we label a photon with the index Λ . a_{Λ}^{\dagger} and a_{Λ} are the creation and annihilation operators of the photon labeled with Λ , respectively, and ε_{Λ} is the photon energy. H_x is expressed by the momentum operator \mathbf{p} and the vector potential \mathbf{A} in the Coulomb gauge:

$$\begin{aligned} H_x &= \sum_{\alpha, \alpha'} \langle \psi_{\alpha} | \left(-\frac{1}{c} \right) (\mathbf{A} \cdot \mathbf{p}) | \psi_{\alpha'} \rangle c_{\alpha}^{\dagger} c_{\alpha'} \\ &= \sum_{\alpha, \alpha'} \sum_{\Lambda} w_{\alpha\alpha'}(\Lambda) c_{\alpha}^{\dagger} c_{\alpha'} a_{\Lambda} + (\text{H.c.}), \end{aligned} \quad (4)$$

where c is the speed of light and its value is about 137 in the Hartree atomic units. The indices α and α' specify each state of the 1s, 2p, or 3d electrons or the photoelectron forming the basis of H_e , which is explained below. ψ_{α} is the electron wave function of the α state. c_{α}^{\dagger} (c_{α}) is the creation (annihilation) operator of the α electron. We apply the dipole approximation to the matrix element w :

$$w_{\alpha\alpha'}(\Lambda) \propto \frac{1}{\sqrt{\varepsilon_{\Lambda}}} \langle \psi_{\alpha} | (\hat{\varepsilon}_{\lambda} \cdot \mathbf{p}) | \psi_{\alpha'} \rangle, \quad (5)$$

where $\hat{\varepsilon}_{\lambda}$ is the polarization vector with the λ polarization.

H_e consists of each Hamiltonian for the 1s, 2p, photoelectron, and band states, and the 2p-3d interaction:

$$H_e = h_{1s} + h_{\bar{p}} + h_{2p} + H_{\text{band}} + V_{pd}. \quad (6)$$

The 1s Hamiltonian h_{1s} and the photoelectron Hamiltonian $h_{\bar{p}}$ are assumed to be

$$h_{1s} = \sum_{\mathbf{k}} \sum_{\sigma} \varepsilon_{1s} (c_{\mathbf{k},\sigma}^{1s})^{\dagger} c_{\mathbf{k},\sigma}^{1s} = \sum_i \sum_{\sigma} \varepsilon_{1s} (c_{i,\sigma}^{1s})^{\dagger} c_{i,\sigma}^{1s}, \quad (7)$$

$$h_{\bar{p}} = \sum_{\mathbf{k}, \mathbf{G}} \sum_{\sigma} \varepsilon_{|\mathbf{k}+\mathbf{G}|} c_{\mathbf{k},\mathbf{G},\sigma}^{\dagger} c_{\mathbf{k},\mathbf{G},\sigma} \equiv \sum_{\mathbf{K}} \sum_{\sigma} \varepsilon_{\mathbf{K}} c_{\mathbf{K},\sigma}^{\dagger} c_{\mathbf{K},\sigma}, \quad (8)$$

where \mathbf{k} , \mathbf{G} , and i indicate a crystal-momentum vector in the first Brillouin zone, a reciprocal lattice vector, and a unit cell,

respectively. The index σ shows the up (\uparrow) or down (\downarrow) spin. $(c_{\mathbf{k},\sigma}^{1s})^{\dagger}$ and $c_{\mathbf{k},\sigma}^{1s}$ are the creation and annihilation operators of the 1s electron with \mathbf{k} and σ , respectively, whereas $(c_{i,\sigma}^{1s})^{\dagger}$ and $c_{i,\sigma}^{1s}$ are the operators represented by i instead of \mathbf{k} . $c_{\mathbf{K},\sigma}^{\dagger}$ and $c_{\mathbf{K},\sigma}$ are the creation and annihilation operators of the photoelectron with the momentum vector \mathbf{K} in the extended zone scheme and the spin σ . The 1s electron energy ε_{1s} does not depend on \mathbf{k} and σ . We assume that the photoelectron energy $\varepsilon_{\mathbf{K}}$ is sufficiently large to consider the photoelectron as a free electron, whose energy does not depend on σ .

The 2p Hamiltonian h_{2p} includes the spin-orbit interaction:

$$h_{2p} = \sum_{\mathbf{k}} \sum_{\zeta, \zeta'} (\varepsilon_{2p} \delta_{\zeta \zeta'} + \varepsilon_{2p}^{\text{soc}} (\mathbf{l} \cdot \mathbf{s})_{\zeta \zeta'}) c_{\mathbf{k},\zeta}^{\dagger} c_{\mathbf{k},\zeta'}, \quad (9)$$

where the indices ζ and ζ' indicate each 2p state. $c_{\mathbf{k},\zeta}^{\dagger}$ and $c_{\mathbf{k},\zeta}$ are the creation and annihilation operators of the 2p electron with \mathbf{k} and ζ , respectively. The 2p energy ε_{2p} does not depend on \mathbf{k} . The spin-orbit interaction is described by the orbital angular momentum vector \mathbf{l} , the spin vector \mathbf{s} , and the coupling energy $\varepsilon_{2p}^{\text{soc}}$.

The band Hamiltonian is taken as a Hubbard-type Hamiltonian:

$$H_{\text{band}} = h_{\text{TB}} + H'_{\text{band}}, \quad (10)$$

where h_{TB} and H'_{band} are the tight-binding Hamiltonian and the on-site Coulomb term, respectively. h_{TB} is given by

$$h_{\text{TB}} = \sum_{i,i'} \sum_{\mu,\mu'} \sum_{\sigma} t_{i\mu,i'\mu'} c_{i,\mu,\sigma}^{\dagger} c_{i',\mu',\sigma}, \quad (11)$$

where the orbital indices μ and μ' include not only 3d states but also 4s and 4p states to reproduce the band structure calculated by an *ab initio* calculation. $c_{i,\mu,\sigma}^{\dagger}$ and $c_{i,\mu,\sigma}$ are the creation and annihilation operators of the electron specified by i , μ , and σ , respectively. $t_{i\mu,i'\mu'}$ is the hopping integral from the orbital μ' in the unit cell i' to the orbital μ in the unit cell i . The hopping integrals are determined by a maximally localized Wannier function method to reproduce the band structure (see Sec. III A). The rest of H_{band} includes Coulomb and exchange energy terms:

$$H'_{\text{band}} = h_U + h_{U'} + h_J, \quad (12)$$

$$h_U = \sum_i \sum_{\mu} U_{\mu} n_{i,\mu,\uparrow} n_{i,\mu,\downarrow}, \quad (13)$$

$$h_{U'} = \frac{1}{2} \sum_i \sum_{\mu \neq \mu'} \sum_{\sigma, \sigma'} U'_{\mu\mu'} n_{i,\mu,\sigma} n_{i,\mu',\sigma'}, \quad (14)$$

$$h_J = \frac{1}{2} \sum_i \sum_{\mu \neq \mu'} \sum_{\sigma, \sigma'} J_{\mu\sigma,\mu'\sigma'} c_{i,\mu,\sigma}^{\dagger} c_{i,\mu',\sigma'}^{\dagger} c_{i,\mu,\sigma'} c_{i,\mu',\sigma}, \quad (15)$$

where $n_{i,\mu,\sigma}$ is the number operator of the electron specified by i , μ , and σ . We treat H_{band} within the MF approximation (see Appendix A). The Coulomb integrals U , U' , and the exchange integral J are chosen to reproduce the real magnetic moment. A two-particle hopping term is not included in H_{band} because it vanishes in the MF approximation. The 2p-3d

interaction V_{pd} is given by

$$V_{pd} = \frac{1}{N} \sum_{\mathbf{k}, \mathbf{k}', \mathbf{q}} \sum_{\zeta, \zeta'} \sum_{\xi, \xi'} v_{\zeta \zeta', \xi \xi'} c_{\mathbf{k}, \zeta}^\dagger c_{\mathbf{k}', \xi}^\dagger c_{\mathbf{k}+\mathbf{q}, \xi'} c_{\mathbf{k}-\mathbf{q}, \zeta'}, \quad (16)$$

where the index ξ indicates each $3d$ state. $c_{\mathbf{k}, \xi}^\dagger$ and $c_{\mathbf{k}, \xi}$ are the creation and annihilation operators of the $3d$ electron specified by \mathbf{k} and ξ , respectively. The momentum \mathbf{q} is transferred between the $2p$ and $3d$ states. N is the number of \mathbf{k} points in the first Brillouin zone. The explicit form of $v_{\zeta \zeta', \xi \xi'}$ is represented by the matrix elements of the electron-electron interaction v_{ee} :

$$v_{\zeta \zeta', \xi \xi'} = \langle \psi_\zeta \psi_\xi | v_{ee} | \psi_{\zeta'} \psi_{\xi'} \rangle - \langle \psi_\zeta \psi_\xi | v_{ee} | \psi_{\xi'} \psi_{\zeta'} \rangle, \quad (17)$$

$$\begin{aligned} & \langle \psi_\zeta \psi_\xi | v_{ee} | \psi_{\zeta'} \psi_{\xi'} \rangle \\ &= \sum_L \frac{4\pi}{2l+1} G(1m_{\zeta'}, L|1m_\zeta) G(2m_\xi, L|2m_{\xi'}) \\ & \quad \times F^l(2p, 3d) \delta_{\sigma_\zeta, \sigma_{\zeta'}} \delta_{\sigma_\xi, \sigma_{\xi'}}, \end{aligned} \quad (18)$$

$$\begin{aligned} & \langle \psi_\zeta \psi_\xi | v_{ee} | \psi_{\xi'} \psi_{\zeta'} \rangle \\ &= \sum_L \frac{4\pi}{2l+1} G(2m_{\xi'}, L|1m_\zeta) G(2m_\xi, L|1m_{\zeta'}) \\ & \quad \times G^l(2p, 3d) \delta_{\sigma_\zeta, \sigma_{\xi'}} \delta_{\sigma_\xi, \sigma_{\zeta'}}, \end{aligned} \quad (19)$$

$$G(L_1, L|L_2) = \int d\hat{\mathbf{r}} Y_{L_2}^*(\hat{\mathbf{r}}) Y_L(\hat{\mathbf{r}}) Y_{L_1}(\hat{\mathbf{r}}), \quad (20)$$

where the angular momentum index L is short-hand notation for (l, m) with the azimuthal quantum number l and the magnetic quantum number m . The Gaunt coefficient $G(L_1, L|L_2)$, defined by the spherical harmonics Y_L, Y_{L_1} , and Y_{L_2} , is numerically calculated. In itinerant electron systems, the Slater-Condon parameters F^l and G^l are generally reduced from their atomic values due to screening effects [33–38]. Because it is difficult to estimate screened values of the parameters precisely, we adjust them to reproduce the observed XMCPE spectra.

C. Transition probability

To describe the transition probability from incident to outgoing photons, it is useful to use the interaction picture of H_x :

$$H_x(t) = e^{iH_0 t} H_x e^{-iH_0 t} = \sum_{\alpha, \alpha'} \sum_{\Lambda} h_{\alpha \alpha'}(t; \Lambda) a_{\Lambda} e^{-i\epsilon_{\Lambda} t} + (\text{H.c.}), \quad (21)$$

$$h_{\alpha \alpha'}(t; \Lambda) = w_{\alpha \alpha'}(\Lambda) c_{\alpha}^\dagger(t) c_{\alpha'}(t), \quad (22)$$

$$h_{\alpha' \alpha}^\dagger(t; \Lambda) = w_{\alpha' \alpha}^*(\Lambda) c_{\alpha}^\dagger(t) c_{\alpha'}(t). \quad (23)$$

The expectation value of the number of outgoing photons at the time t_0 is given by an interaction picture of wave function Ψ .

$$\langle n_{\Lambda_f} \rangle_{t_0}(\Lambda_i) = \langle \Psi_I(t_0; \Lambda_i) | a_{\Lambda_f}^\dagger a_{\Lambda_f} | \Psi_I(t_0; \Lambda_i) \rangle, \quad (24)$$

where the incident and outgoing photon states are specified by the indices Λ_i and Λ_f , respectively. We focus our attention on

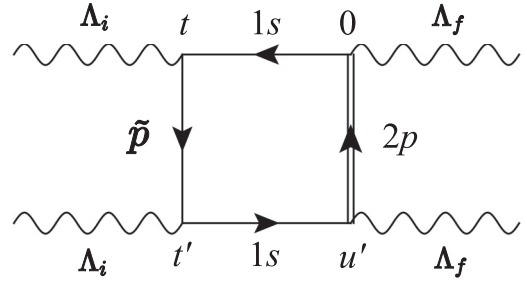


FIG. 2. Keldysh diagram for a $K\alpha$ XMCPE process. The times t and 0 belong to the $+$ leg, whereas the times t' and u' belong to the $-$ leg, as defined in Ref. [39]. The wavy lines correspond to the incident photon states labeled with Λ_i or the outgoing photon state labeled with Λ_f . The horizontal lines describe $1s$ states, and the downward line indicates a free electron state denoted by \tilde{p} . The upward double line indicates a $2p$ state accompanied by $3d$ electron excitations.

a photon-in-photon-out state in the state Ψ_I :

$$\begin{aligned} |\Psi_I(t_0; \Lambda_i)\rangle &\approx \left(\frac{1}{i}\right)^2 \sum_{\alpha, \alpha'} \sum_{\beta, \beta'} \sum_{\Lambda, \Lambda'} \int_{-\infty}^{t_0} du \int_{-\infty}^u dt \\ &\quad \times (h_{\alpha' \alpha}^\dagger(u; \Lambda') a_{\Lambda'}^\dagger e^{i\epsilon_{\Lambda'} u}) \\ &\quad \times (h_{\beta \beta'}(t; \Lambda') a_{\Lambda'} e^{-i\epsilon_{\Lambda'} t}) a_{\Lambda_i}^\dagger |0\rangle, \end{aligned} \quad (25)$$

where $|0\rangle$ corresponds to the ground state.

Thus, the transition probability W_{fi} from the photon state Λ_i to Λ_f is given by the time derivative of the number of outgoing photons:

$$\begin{aligned} W_{fi} &= \left. \frac{d\langle n_{\Lambda_f} \rangle(\Lambda_i)}{dt_0} \right|_{t_0 \rightarrow \infty} \\ &= \frac{1}{\hbar^4} \int_{-\infty}^0 dt \int_{-\infty}^{\infty} du' \int_{-\infty}^{\infty} dt' \\ &\quad \times S(t, 0, u', t') e^{i\epsilon_i(t'-t)} e^{-i\epsilon_f u'}, \end{aligned} \quad (26)$$

where ϵ_i and ϵ_f are the photon energies with Λ_i and Λ_f , respectively. $S(t, u, u', t')$ depending on the times t, u, u' , and t' is the S matrix, defined as follows [39]:

$$\begin{aligned} S(t, u, u', t') &= \langle 0 | h_{\beta_1 \beta_1}^\dagger(t'; \Lambda_i) h_{\alpha_1 \alpha_1}(u'; \Lambda_f) \\ &\quad \times h_{\alpha_2 \alpha_2}^\dagger(u; \Lambda_f) h_{\beta_2 \beta_2}(t; \Lambda_i) | 0 \rangle. \end{aligned} \quad (27)$$

To describe a $K\alpha$ XMCPE process, we use a Keldysh diagram for the S matrix (Fig. 2). In accordance with Ref. [39], the upper and lower horizontal lines in Fig. 2 belong to the $+$ and $-$ branches, respectively. The $-$ branch corresponds to the complex conjugate of the $+$ branch, and the diagrammatic connection between the two branches provides the excitation or relaxation processes. Figure 2 shows that the incident photon with Λ_i creates a hole in the $1s$ states, which is accompanied by electron excitation from the $1s$ to \tilde{p} states at the time t . After the time evolution of the $1s$ hole state from the time t to 0 , the $1s$ hole is relaxed and buried by a $2p$ electron at the time 0 , which is accompanied by the emission of the outgoing photon with Λ_f . The same kind of diagram was calculated in Ref. [6]. However, we also include the relaxation process

involving $3d$ electron excitations, which was not considered in Ref. [6].

The expression for the S matrix corresponding to the diagram is

$$S(t, 0, u', t') = -i^4 \sum_{\mathbf{k}, \zeta} \sum_{\mathbf{k}', \zeta'} \sum_{\bar{\mathbf{k}}} \sum_{\sigma} [w] \\ \times G_{\mathbf{k}\zeta, \mathbf{k}'\zeta'}^{+,2p}(0, u') \tilde{G}_{\sigma}^{c,1s}(u', t') \\ \times G_{\bar{\mathbf{k}}\sigma}^{-,\bar{p}}(t', t) G_{\sigma}^{c,1s}(t, 0), \quad (28)$$

$$[w] = (w_{\bar{\mathbf{k}}}^{\bar{p},1s}(\Lambda_i))^* w_{\mathbf{k}\zeta, \sigma}^{2p,1s}(\Lambda_f) (w_{\mathbf{k}'\zeta', \sigma}^{2p,1s}(\Lambda_f))^* w_{\bar{\mathbf{k}}}^{\bar{p},1s}(\Lambda_i). \quad (29)$$

We derive the above expression based on the fact that all the dipole transition matrices have the same spin index (see Appendix B). Each Green's function is defined as follows [39,40].

$$G_{\alpha, \beta}^c(t, t') = \frac{1}{i} \langle T[c_{\alpha}(t), c_{\beta}^{\dagger}(t')] \rangle, \quad (30)$$

$$\tilde{G}_{\alpha, \beta}^c(t, t') = \frac{1}{i} \langle \tilde{T}[c_{\alpha}(t), c_{\beta}^{\dagger}(t')] \rangle, \quad (31)$$

$$G_{\alpha, \beta}^{+}(t, t') = -\frac{1}{i} \langle c_{\alpha}^{\dagger}(t') c_{\beta}(t) \rangle, \quad (32)$$

$$G_{\alpha, \beta}^{-}(t, t') = \frac{1}{i} \langle c_{\alpha}(t) c_{\beta}^{\dagger}(t') \rangle, \quad (33)$$

$$G_{\alpha}(t, t') \equiv G_{\alpha, \alpha}(t, t'). \quad (34)$$

Here, T (\tilde{T}) is the time-ordering (anti-time-ordering) operator. Since h_{1s} and $h_{\bar{p}}$ are already diagonal, $G^{c,1s}$, $\tilde{G}^{c,1s}$, and $G^{-,\bar{p}}$ can be written exactly. However, calculating $G^{+,2p}$ requires some approximation because V_{pd} gives off-diagonal components in the $2p$ - $3d$ basis space. Here, the inverse Fourier transform of $G^{+,2p}$ is defined as

$$G^{+,2p}(0, u') = \int_{-\infty}^{\infty} \frac{d\omega}{2\pi} G^{+,2p}(\omega) e^{-i\omega(0-u')}. \quad (35)$$

By performing the time integrations in Eq. (26),

$$W_{fi} \propto \sum_{\mathbf{k}, \zeta} \sum_{\mathbf{k}', \zeta'} \sum_{\sigma} w_{\mathbf{k}\zeta, \sigma}^{2p,1s}(\Lambda_f) (w_{\mathbf{k}'\zeta', \sigma}^{2p,1s}(\Lambda_f))^* \\ \times \int_{-\infty}^{\infty} \frac{d\omega}{2\pi} (-iG_{\mathbf{k}\zeta, \mathbf{k}'\zeta'}^{+,2p}(\omega)) \frac{|w_{\bar{\mathbf{k}}}^{\bar{p},1s}(\Lambda_i)|^2 \rho_0(\omega_{\bar{\mathbf{k}}})}{(\omega - \varepsilon_{1s} - \varepsilon_f)^2 + \eta^2}, \quad (36)$$

$$\omega_{\bar{\mathbf{k}}} = \omega + \varepsilon_i - \varepsilon_f, \quad (37)$$

where ρ_0 is the free electron density of states. The convergence factor η ($\rightarrow 0+$) can be replaced by Γ_{1s} for a lifetime broadening of a $1s$ core hole. The integral range in Eq. (36) is practically replaced by an energy range where $G^{+,2p}$ does not vanish. We define the center and width of the energy range as $\bar{\omega}$ and $\Delta\omega$, respectively. Because of the Lorentzian in Eq. (36), the energy difference $(\bar{\omega} - \varepsilon_f)$ can be approximated to ε_{1s} (< 0). Moreover, ω_i is fixed in the XMCPPE process. Thus, ρ_0 and $|w_{\bar{\mathbf{k}}}^{\bar{p},1s}|^2$ can be factored out and regarded as a constant, denoted by C_i , when the photoelectron frequency $\omega_{\bar{\mathbf{k}}} (\approx \varepsilon_i - |\varepsilon_{1s}|)$ is sufficiently larger than $\Delta\omega$. Therefore, W_{fi}

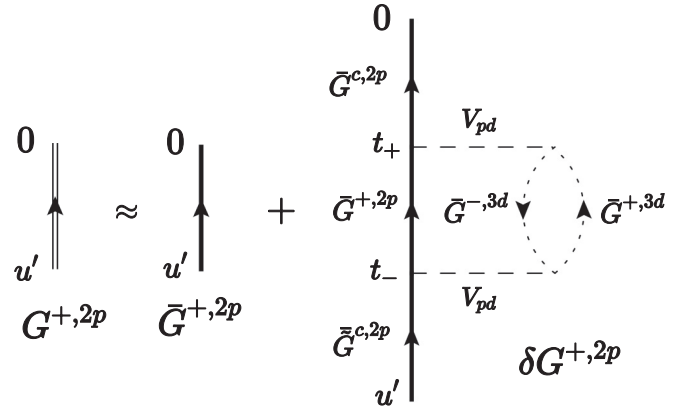


FIG. 3. Diagrams illustrating the approximation for the full $2p$ Green's function G^{2p} . The oriented double line indicates G^{2p} , and the oriented bold lines correspond to the MF $2p$ Green's function \bar{G}^{2p} . The oriented dotted lines indicate the MF $3d$ Green's function \bar{G}^{3d} . The dashed lines correspond to the $2p$ - $3d$ interaction V_{pd} . $\delta G^{+,2p}$ is the correction to $\bar{G}^{+,2p}$ by $3d$ electron excitations. The times 0 and t_+ belong to the $+$ leg, whereas the times t_- and u' belong to the $-$ leg. The type of each Green's function is determined by the legs to which its two time variables belong.

is given as follows.

$$W_{fi} \propto C_i \sum_{\mathbf{k}, \zeta} \sum_{\mathbf{k}', \zeta'} \sum_{\sigma} w_{\mathbf{k}\zeta, \sigma}^{2p,1s}(\Lambda_f) (w_{\mathbf{k}'\zeta', \sigma}^{2p,1s}(\Lambda_f))^* \\ \times \int_{\bar{\omega}-\Delta\omega/2}^{\bar{\omega}+\Delta\omega/2} \frac{d\omega}{2\pi} (-iG_{\mathbf{k}\zeta, \mathbf{k}'\zeta'}^{+,2p}(\omega)) \frac{1}{(\omega - \varepsilon_{1s} - \varepsilon_f)^2 + \Gamma_{1s}^2}. \quad (38)$$

D. $2p$ Green's function

We approximate the $2p$ Green's function $G^{+,2p}$ by the MF function $\bar{G}^{+,2p}$ and the single-bubble correction $\delta G^{+,2p}$ (Fig. 3):

$$G^{+,2p} \approx \bar{G}^{+,2p} + \delta G^{+,2p}, \quad (39)$$

$$W \approx \bar{W} + \delta W. \quad (40)$$

$\delta G^{+,2p}$ includes excitations in the $3d$ bands induced by V_{pd} , which corresponds to the first Born approximation.

The MF $2p$ Green's functions $\bar{G}^{+,2p}$, $\bar{G}^{c,2p}$, and $\bar{G}^{c,2p}$ can be calculated by using the eigenvalues of the MF $2p$ Hamiltonian, defined as \bar{H}_{2p} :

$$\bar{H}_{2p} \equiv h_{2p} + \sum_{\mathbf{k}, \mathbf{q}} \sum_{\zeta_i, \xi_i} v_{\zeta_i \zeta_2, \xi_1 \xi_2} n_{\xi_1, \xi_2}(\mathbf{q}) c_{\mathbf{k}, \zeta_1}^{\dagger} c_{\mathbf{k}-\mathbf{q}, \zeta_2}, \quad (41)$$

$$n_{\xi_1, \xi_2}(\mathbf{q}) = \frac{1}{N} \sum_{\mathbf{k}'} \langle c_{\mathbf{k}', \xi_1}^{\dagger} c_{\mathbf{k}'+\mathbf{q}, \xi_2} \rangle_{\text{band}}. \quad (42)$$

The expectation value $\langle \dots \rangle_{\text{band}}$ is taken in the ground state of the band electron system described by the MF band Hamiltonian \bar{H}_{band} (see Appendix A). In the MF approximation, $n_{\xi_1, \xi_2}(\mathbf{q})$ does not vanish only when $\mathbf{q} = \mathbf{0}$, which provides that the eigenvalues of \bar{H}_{2p} are independent from \mathbf{k} . By using the definition of G^+ in Eq. (32) and the inverse Fourier

transform in Eq. (35),

$$\bar{H}_{2p} = \sum_{\mathbf{k}} \sum_a E_a c_{\mathbf{k},a}^\dagger c_{\mathbf{k},a}, \quad (43)$$

$$\begin{aligned} -i\bar{G}_{\mathbf{k}\zeta, \mathbf{k}'\zeta'}^{+,2p}(\omega) &= \delta_{\mathbf{k},\mathbf{k}'} (-i\bar{G}_{\zeta, \zeta'}^{+,2p}(\omega)) \\ &= \delta_{\mathbf{k},\mathbf{k}'} \sum_a u_\zeta^a (-i\bar{G}_a^{+,2p}(\omega)) (u_{\zeta'}^a)^* \\ &= \delta_{\mathbf{k},\mathbf{k}'} \sum_a u_\zeta^a (2\pi \delta(\omega - E_a)) (u_{\zeta'}^a)^*, \end{aligned} \quad (44)$$

$$c_\zeta = \sum_a u_\zeta^a c_a, \quad (45)$$

where the index a denotes each eigenstate of \bar{H}_{2p} . c_a^\dagger and c_a are the creation and annihilation operators of the $2p$ electron with the a state, respectively. We generalize Eq. (44) to include a $2p$ core-hole lifetime effect by replacing the delta function to a Lorentzian:

$$-i\bar{G}_a^{+,2p}(\omega) \equiv 2\pi \left(\frac{1}{\pi} \frac{\Gamma_{2p}}{(\omega - E_a)^2 + \Gamma_{2p}^2} \right). \quad (46)$$

When we take the limit $\Gamma_{2p} \rightarrow 0$, the Lorentzian correctly reproduces the delta function.

From Fig. 3, $\delta G^{+,2p}$ is given by

$$\begin{aligned} -i\delta G_{\mathbf{k}\zeta, \mathbf{k}'\zeta'}^{+,2p}(0, u') &= \left(\frac{1}{i} \right)^2 \frac{1}{N^2} \sum_{\zeta_i} \sum_{\xi_i} \sum_{\mathbf{k}_i, \mathbf{k}'_i} \sum_{\mathbf{q}_+, \mathbf{q}_-} \\ &\times \int_{-\infty}^{\infty} dt_+ dt_- v_{\zeta_1 \zeta_2, \xi_1 \xi_2} v_{\zeta_3 \zeta_4, \xi_3 \xi_4} \\ &\times [\bar{G}^{2p}](0, u') [G^{\pm, 3d}](t_+, t_-), \end{aligned} \quad (47)$$

$$\begin{aligned} [\bar{G}^{2p}](0, u') &= (i\bar{G}_{\mathbf{k}, \zeta; \mathbf{k}_1, \zeta_1}^{c, 2p}(0, t_+)) (-i\bar{G}_{\mathbf{k}_1 - \mathbf{q}_+, \zeta_2; \mathbf{k}_2, \zeta_3}^{+, 2p}(t_+, t_-)) \\ &\times (i\bar{G}_{\mathbf{k}_2 - \mathbf{q}_-, \zeta_4; \mathbf{k}', \zeta'}^{c, 2p}(t_-, u')), \end{aligned} \quad (48)$$

$$\begin{aligned} [\bar{G}^{\pm, 3d}](t_+, t_-) &= (-i\bar{G}_{\mathbf{k}'_1 + \mathbf{q}_+, \xi_2; \mathbf{k}'_2, \xi_3}^{+, 3d}(t_+, t_-)) \\ &\times (i\bar{G}_{\mathbf{k}'_2 + \mathbf{q}_-, \xi_4; \mathbf{k}'_1, \xi_1}^{-, 3d}(t_-, t_+)). \end{aligned} \quad (49)$$

The MF $3d$ Green's functions $\bar{G}^{+, 3d}$ and $\bar{G}^{-, 3d}$ are calculated by using the eigenvalues of \bar{H}_{band} . Taking the explicit expression of the Green's functions and the inverse Fourier transform, we obtain

$$\begin{aligned} -i\delta G_{\mathbf{k}\zeta, \mathbf{k}'\zeta'}^{+,2p}(\omega) &= \delta_{\mathbf{k},\mathbf{k}'} (-i\delta G_{\zeta, \zeta'}^{+,2p}(\omega)) \\ &= \delta_{\mathbf{k},\mathbf{k}'} \sum_{a_1, a_3} u_\zeta^{a_1} (-i\delta G_{a_1, a_3}^{+,2p}(\omega)) (u_{\zeta'}^{a_3})^* \\ &= \left(\frac{1}{i} \right)^2 \delta_{\mathbf{k},\mathbf{k}'} \sum_{a_1} \sum_{\xi_i} u_\zeta^{a_1} V_{\xi_1 \xi_2}^{a_1, a_2} V_{\xi_3 \xi_4}^{a_2, a_3} (u_{\zeta'}^{a_3})^* \\ &\times \Pi_{\xi_2 \xi_3, \xi_4 \xi_1}(E_{a_2} - \omega) \frac{1}{\omega - E_{a_1} - i\Gamma_{2p}} \frac{1}{\omega - E_{a_3} + i\Gamma_{2p}}, \end{aligned} \quad (50)$$

$$V_{\xi, \xi'}^{a, d} = \sum_{\zeta_i} (u_{\zeta_i}^a)^* v_{\zeta_1 \zeta_2, \xi \xi'} u_{\zeta_2}^d. \quad (51)$$

Here note that the \mathbf{k} dependence of $\bar{G}^{+, 2p}$ and $\delta G^{+, 2p}$ vanishes. $V_{\xi, \xi'}^{a, d}$ describes the conservation of angular momentum during the $2p$ hole transition and the excitations in the $3d$ bands. The single-bubble polarization function $\Pi_{\xi_2 \xi_3, \xi_4 \xi_1}(\omega)$ is expressed by the convolution of the $3d$ density of states as

$$\Pi_{\xi_2 \xi_3, \xi_4 \xi_1}(\omega) = 2\pi \int_{-\infty}^{\infty} dE D_{\xi_2 \xi_3}^{\text{hole}}(E) D_{\xi_4 \xi_1}^{\text{particle}}(E + \omega), \quad (52)$$

$$D_{\xi_2 \xi_3}^{\text{hole}}(E) = D_{\xi_2 \xi_3}(E) f(E), \quad (53)$$

$$D_{\xi_4 \xi_1}^{\text{particle}}(E + \omega) = D_{\xi_4 \xi_1}(E + \omega) (1 - f(E + \omega)), \quad (54)$$

$$\begin{aligned} D_{\xi \xi'}(E) &= \frac{1}{N} \sum_{\mathbf{k}, \gamma, \sigma} u_{\xi}^{\mathbf{k}, \gamma, \sigma} (u_{\xi'}^{\mathbf{k}, \gamma, \sigma})^* \\ &\times \left[-\frac{1}{\pi} \text{Im} \left(\frac{1}{E - E_{\mathbf{k}\gamma\sigma} + i\eta_D} \right) \right], \end{aligned} \quad (55)$$

where the index γ indicates each eigenstate of H_{band} within the MF approximation (see Appendix A). D^{hole} and D^{particle} are occupied and unoccupied $3d$ density of states, respectively. To define D^{hole} and D^{particle} , the Fermi distribution function $f(E)$ is included. In practice, the broadening parameter η_D for the density of states is taken as a sufficiently small positive.

We make a remark about the possibility of sum-rule analysis for $K\alpha$ XMCPE based on our formalism. The sum rule analysis in $L_{2,3}$ -edge XMCD has succeeded to obtain the d components of spin and orbital magnetic moments in the absorbing atom separately. The basic idea of the sum rule is that integrals of $L_{2,3}$ -edge x-ray absorption spectra with respect to the photon energy is approximately proportional to the number of unoccupied d electrons. In contrast, integrals of $K\alpha$ XMCPE spectra cannot be related to the number of $3d$ electrons due to the combination of Π and $(\omega - E_a \pm i\Gamma_{2p})^{-1}$ shown in Eq. (50). Detailed investigation of the possibility of sum rule in XMCPE is remaining as a future work.

III. APPLICATION TO METALLIC IRON

A. Parameter settings for numerical calculation

Here we present our procedure and parameters for calculating $K\alpha$ XMCPE in metallic iron. The band structure without spin polarization of BCC iron is calculated by WIEN2K code [41]. The lattice constant is set to 2.866 Å. The generalized gradient approximation with the Perdew-Burke-Ernzerhof functional is used as an effective exchange-correlation functional [42]. By using the calculated band structure, h_{TB} is obtained by WANNIER90 code [43]. The spin-polarized band structure and unitary matrices between the band and $3d$ -orbital states are obtained by diagonalizing \bar{H}_{band} [see Eq. (A10) in Appendix A]. To reproduce the typical magnetic moment of $2.0 \mu_B$ for BCC iron [2], the Coulomb and exchange integrals U , U' , and J for the $3d$ orbitals are set to 2.20, 1.32, and 0.44 eV, respectively. The broadening parameter η_D for the density of states is set to 0.001 eV as a sufficiently small value. The number of \mathbf{k} points N is set to $40 \times 40 \times 40$. The temperature is set to zero, and thus the Fermi distribution function is treated as a step function.

The Slater-Condon parameters F^l and G^l are set to fit the calculated spectra optimally to the observed spectra [44]

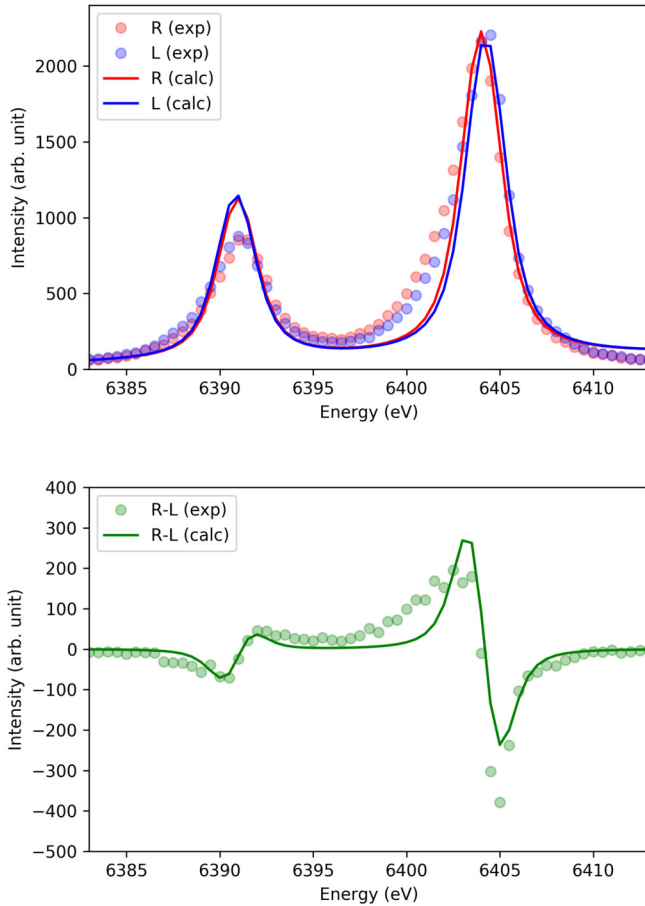


FIG. 4. Calculated emission spectra (upper panel) and their difference (lower panel) including only the \bar{W} term, neglecting the correction δW . In the upper panel, the red and blue solid lines correspond to the right and left circularly polarized emissions, respectively. The Slater-Condon parameters F^0 and G^1 are set to 2.0 eV, and the others are set to zero. The experimental spectra are plotted with circles.

as $(F^0, F^2; G^1, G^3) = (2.0, 0.0; 2.0, 0.0)$ in units of eV. We investigate the dependence of the XMCPE spectra on the parameters in Sec. III C. The spin-orbit interaction $\varepsilon_{2p}^{\text{soc}}$ in the $2p$ states is set to 8.8 eV, which is slightly larger than that of 8.2 eV obtained by the atomic calculation with a $2p$ hole [45], to fit to the observed spectra. The half width at half maximum, $\Gamma_{1s}(\Gamma_{2p})$, for the lifetime broadening of the $1s(2p)$ state is set to 0.7 (0.18) eV [46]. ε_{1s} and ε_{2p} are set to 7118 and 715 eV, respectively, based on x-ray photoemission spectra of α -Fe₂O₃ [47]. In practice, these energies are adjusted to fit to the observed spectra because the energies of α -Fe₂O₃ could differ from those of metallic iron [27]. The emission energy in $K\alpha$ XMCPE includes $\varepsilon_{2p} - \varepsilon_{1s}$ as a constant part. Therefore, the deviation in ε_{1s} and ε_{2p} from those of α -Fe₂O₃ does not affect the shapes of the emission spectra because it only shifts the emission energy of the spectra.

The emission angle β with respect to the magnetization direction (see Appendix B) is set to 60°, consistent with the experimental setting [44]. We investigate emission angle dependence by changing β in Sec. III D. The calculated spectra are also convoluted by a Gaussian to include broadening by

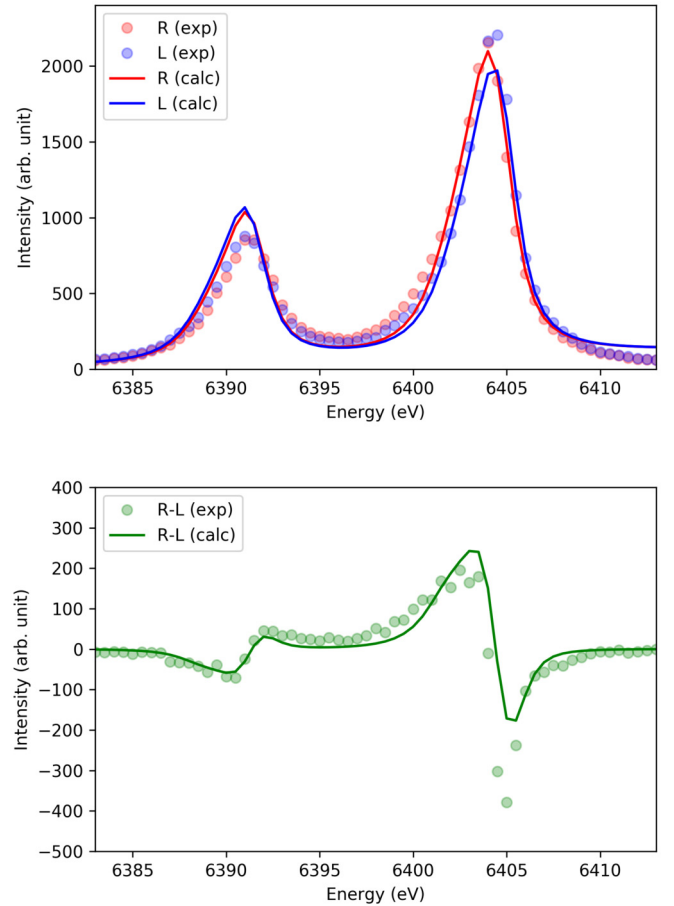


FIG. 5. Calculated emission spectra (upper panel) and their difference (lower panel) obtained from the total W including the correction δW . In the upper panel, the red and blue solid lines correspond to the right and left circularly polarized emissions, respectively. The Slater-Condon parameters F^0 and G^1 are set to 2.0 eV, and the others are set to zero. The experimental spectra are plotted with circles.

experimental resolution and a thermal effect. Here, the half width at half maximum of the Gaussian is defined by Γ_g . The spectral background is approximated and fitted by a linear function and the intensity of the spectra is scaled to fit to the observed spectra. In this paper, we define the right and left circular polarization as the positive and negative light helicity, respectively.

B. Effects of excitations in $3d$ bands

First, we compare the bare spectra \bar{W} in Eq. (40) with the observed spectra [44] (Fig. 4). The Gaussian broadening with Γ_g of 0.68 eV is set to fit the high-energy-side slopes in each calculated emission peak to the observed slopes. The Slater-Condon parameters F^0 and G^1 are set to 2.0 eV, and the others are set to zero for simplicity. The \bar{W} term includes only the direct transitions from the discrete $2p$ to $1s$ states whose energies are calculated in a framework of the one-electron picture. In both panels of Fig. 4, the calculated spectra show symmetric structures around the $K\alpha_1$ (6404 eV) and $K\alpha_2$ (6391 eV) emission peaks. Consequently, in the upper panel of Fig. 4 the calculated spectra cannot reproduce the tail

shape on the low-energy side of each peak, and in the lower panel of Fig. 4 the large discrepancy between the calculated and experimental spectra appears around 6400 eV where the observed tail structure is pronounced.

Figure 5 shows the calculated spectra using the total W . The same Slater-Condon parameters are used as in Fig. 4, whereas the scale factor and $\Gamma_g (= 0.57$ eV) in Fig. 5 are different from those in Fig. 4 to fit to the observed spectra. The upper panel in Fig. 5 shows an improvement in the agreement between the calculated and observed tail shapes around 6401 and 6388 eV. The calculated spectra also show an improvement in the difference around 6399 eV in the lower panel of Fig. 5. Therefore, the effects of the excitations included in δW are important to reproduce the observed XMCPE spectra.

Figure 6 shows the contributions from \bar{W} and δW to the total W . The results show that the origin of the tail shapes is the overlap of the \bar{W} and δW peaks. To understand how each peak appears, we suppress the broadening effects on the calculations. Figure 7 shows the \bar{W} and δW terms separately around the $K\alpha_1$ emission calculated with the same parameters as in Figs. 5 and 6, except for the reduced lifetime broadening parameter $\Gamma (= \Gamma_{1s} = \Gamma_{2p})$ and no Gaussian broadening. The \bar{W} term with $\Gamma = 0.01$ eV shows four sharp peaks in each panel of Fig. 7. As shown in Eq. (44), the relative peak positions correspond to $2p_{3/2}$ sublevel energies. The calculations with $\Gamma = 0.1$ eV show that these peaks are smeared into a single peak due to the lifetime broadening. On the other hand, the δW term has a continuum, even with $\Gamma = 0.01$ eV, in addition to peak structures. This continuum contribution arises from the broad dispersion of the $3d$ bands. Although the peak structures of δW with $\Gamma = 0.01$ eV appear stronger than the continuum contribution, the broadening effect rapidly damps the sharp peaks and makes the continuum contribution dominant, as shown by the calculation with $\Gamma = 0.1$ eV. Finally, the original larger lifetime broadening of $\Gamma_{1s} = 0.7$ eV merges all structures of δW with $\Gamma = 0.1$ eV into the single $K\alpha_1$ peak shown in Fig 6.

C. Dependence of XMCPE spectra on the Slater-Condon parameters

Figures 8 and 9 show the dependence on the Slater-Condon parameters of ($F^0, F^2; G^1, G^3$) for the \bar{W} and δW terms, respectively. The horizontal axes show the difference between the total energy and ($\varepsilon_{2p} - \varepsilon_{1s}$).

While the same values of Γ_{1s} and Γ_{2p} in Figs. 4 and 5 are used in Figs. 8 and 9, the Gaussian broadening is not included. A scale factor is fixed in Figs. 8 and 9 for easy comparison. The atomic Slater-Condon parameters of (2.0, 7.4; 4.2, 3.1) in units of eV are obtained by a Hartree-Fock calculation of an Fe ion with the configuration of ($2p^5, 3d^6$) [45]. The optimized Slater-Condon parameters are defined as (2.0, 0.0; 2.0, 0.0), which are used in Figs. 4 and 5. The reduction of the optimized values compared with the atomic values can be interpreted as screening effects [37,38]. The values of the optimized parameters may change beyond the present lowest-order approximation (the Born approximation), for example, using the ladder approximation (i.e., the T -matrix approximation).

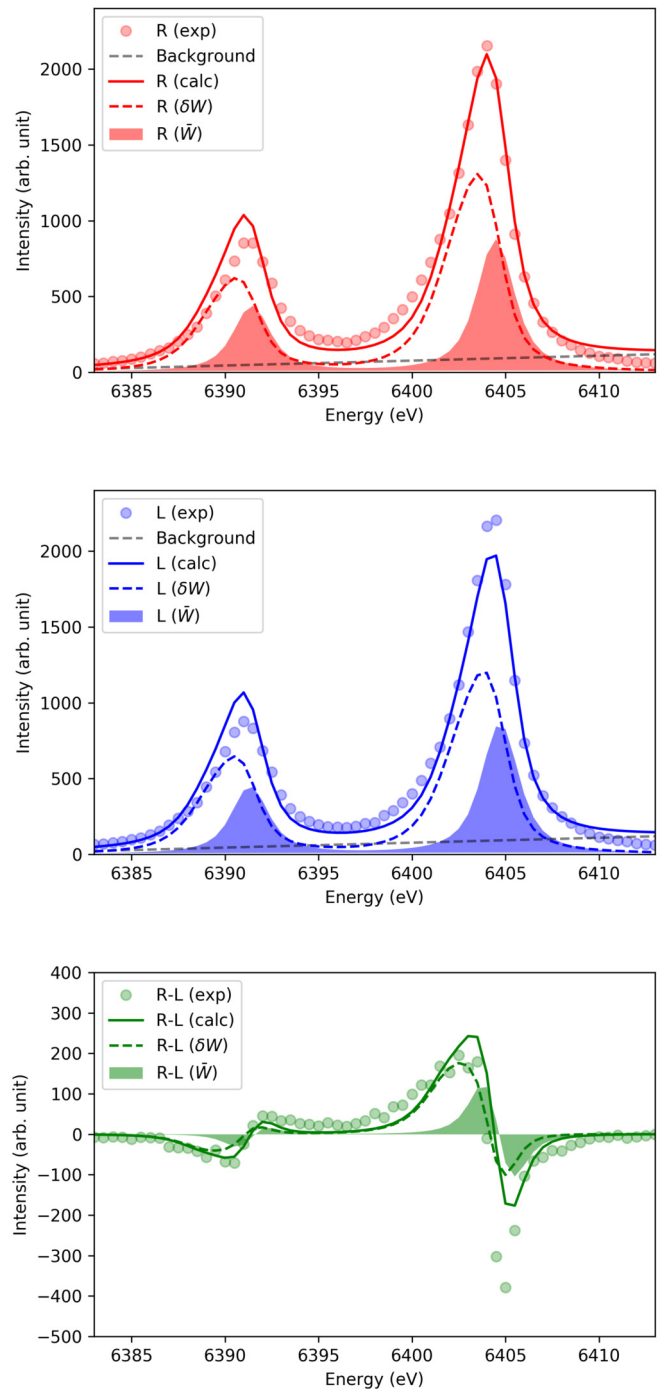


FIG. 6. Contributions from \bar{W} and δW to the total W . Right and left circularly polarized emission spectra are, respectively, shown in the upper and middle panels, and their difference is in the lower panel. The total W results are shown by solid lines. The \bar{W} and δW terms are shown as filled areas and dashed lines, respectively. The background is approximated by a linear function shown as gray dashed lines. The experimental spectra are plotted with circles.

To understand effects of F^2 and G^3 , we focus on calculations with (2.0, 7.4; 2.0, 3.1) and (2.0, 0.0; 4.0, 0.0). The two of the \bar{W} curves in Fig. 8 show almost the same contribution, indicating that the effects of F^2 and G^3 can be replaced by the effects of G^1 . Although the peak intensity of δW with

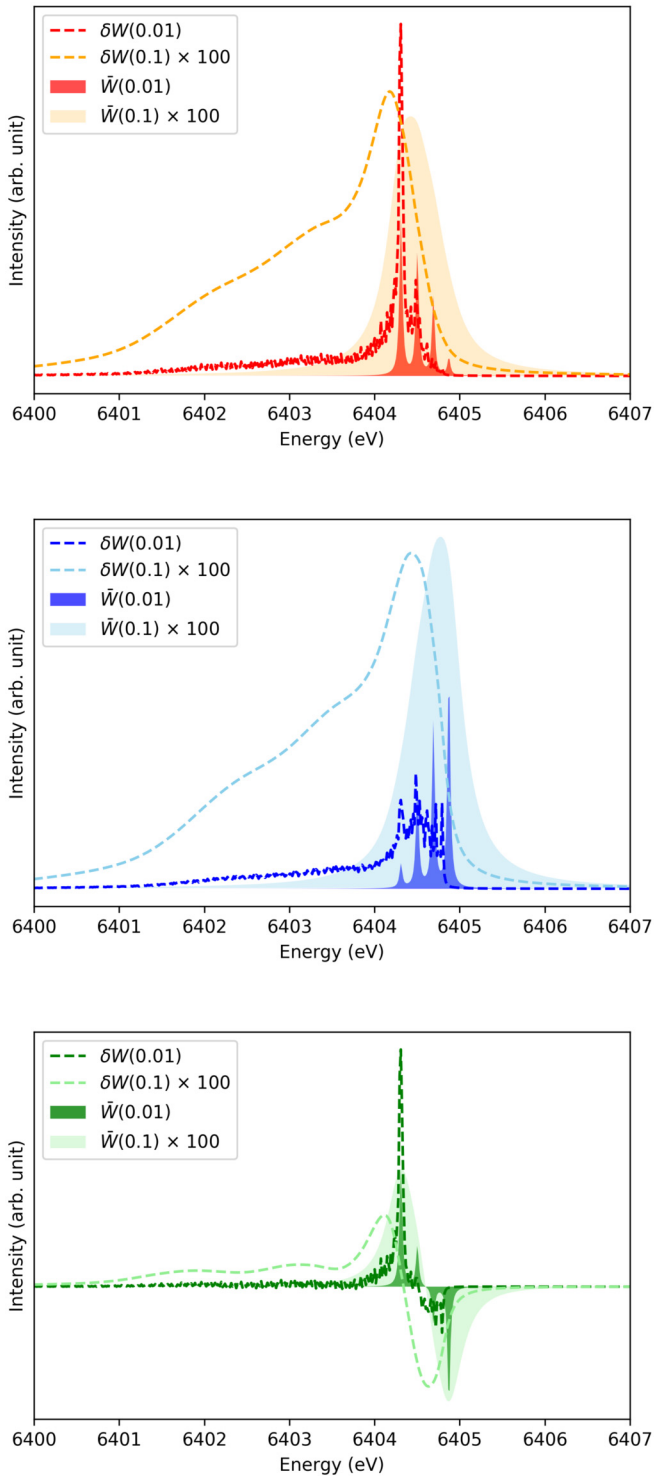


FIG. 7. Calculated right (upper panel) and left (middle panel) circularly polarized emissions and their difference (lower panel) around the $K\alpha_1$ emission with the same parameters as in Figs. 5 and 6 except for the reduced lifetime broadening parameter $\Gamma (= \Gamma_{1s} = \Gamma_{2p})$ and no Gaussian broadening. The \bar{W} and δW terms are shown as filled areas and dashed lines, respectively. The dark (light) lines or filled areas correspond to the results for $\Gamma = 0.01$ ($\Gamma = 0.1$). The intensity of each term with Γ of 0.1 is multiplied by scale factors for easy comparison.

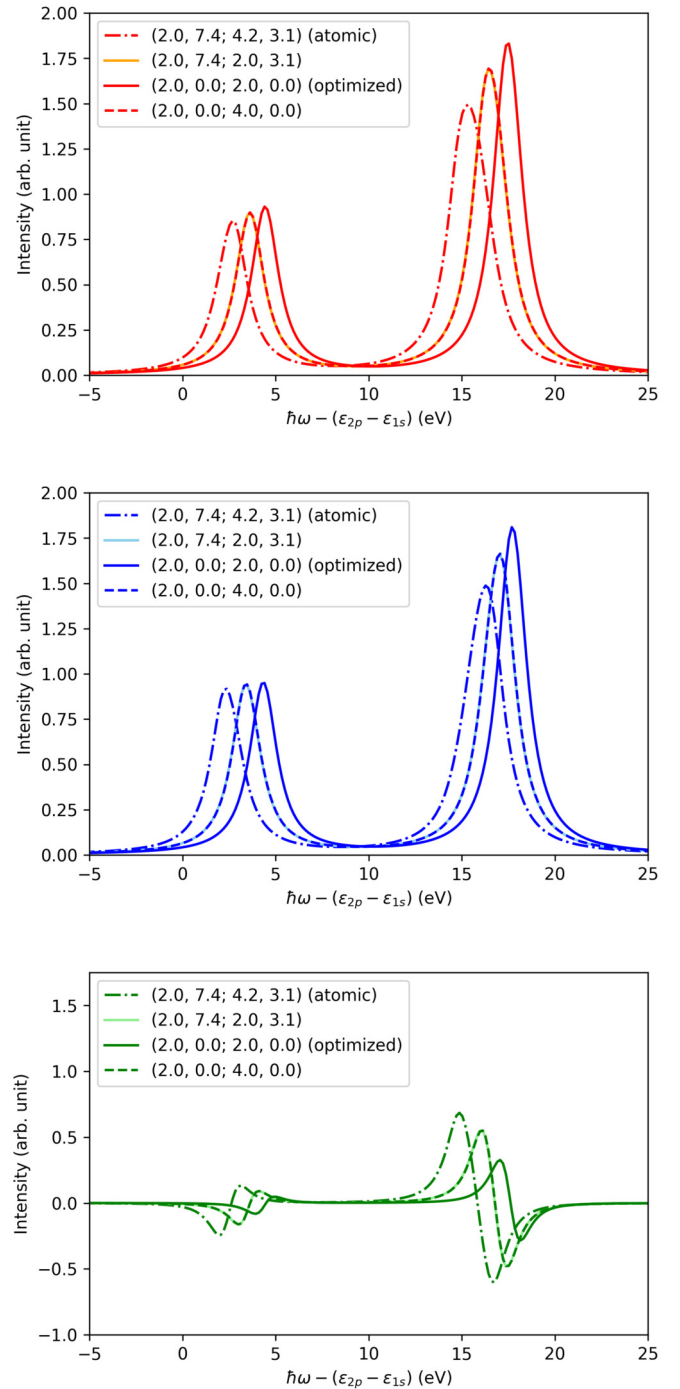


FIG. 8. Calculated right (upper panel) and left (middle panel) circular polarization terms and their difference (lower panel) using only \bar{W} with various Slater-Condon parameters of $(F^0, F^2; G^1, G^3)$ in units of eV without Gaussian broadening. The atomic values of the parameters (2.0, 7.4; 4.2, 3.1) are obtained by a Hartree-Fock calculation [45]. The optimized parameters are the same as those used in Fig. 5. The calculations with (2.0, 7.4; 2.0, 3.1) (light solid line) and (2.0, 0.0; 4.0, 0.0) (dark dashed line) show almost the same contributions.

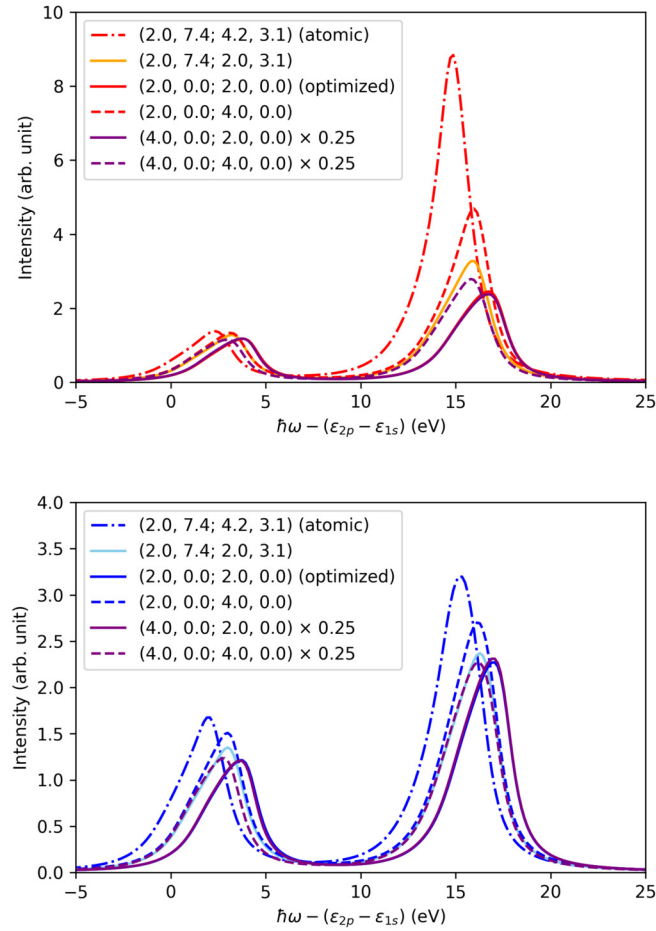


FIG. 9. Calculated right (upper panel) and left (middle panel) circular polarization terms using only δW for various sets of Slater-Condon parameters (F^0 , F^2 ; G^1 , G^3) in units of eV without Gaussian broadening. The calculated curves with F^0 of 4.0 eV (purple lines) are horizontally shifted to fit to the curves with F^0 of 2.0 eV, and are multiplied by 0.25 for scaling.

(2.0, 7.4; 2.0, 3.1) is smaller than that with (2.0, 0.0; 4.0, 0.0) in Fig. 9, most of the effects of F^2 and G^3 can also be reproduced by those of G^1 for δW . Furthermore, F^2 of 7.4 eV is not dominant, and the parameter sets (G^1 , G^3) of (2.0, 3.0) and (4.0, 0.0) have a similar effect (results not shown). These results justify our setting of F^2 and G^3 to zero for simplicity in Figs. 4 and 5.

Next, to understand the effects of G^1 , we focus on comparing (2.0, 7.4; 4.2, 3.1) with (2.0, 7.4; 2.0, 3.1), and (2.0, 0.0; 4.0, 0.0) with (2.0, 0.0; 2.0, 0.0). In Figs. 8 and 9, the smaller value of G^1 provides the higher peak energy positions because the interactions including F^1 and G^1 are summed with opposite signs in Eq. (17). The smaller G^1 value also provides the larger \bar{W} intensity in the top and middle panels of Fig. 8, but the smaller difference intensity of \bar{W} in the bottom panel, owing to the smaller exchange split of the $2p$ sublevels. On the other hand, the smaller G^1 value provides the smaller δW intensity in Fig. 9 because the reduction of G^1 decreases the intensity of the excitations in the $3d$ bands. Although not shown in Fig. 9, the smaller G^1 value provides the smaller difference intensity of δW , analogous to that of \bar{W} .

TABLE I. Effects of each Slater-Condon parameter on the \bar{W} and the δW term with respect to their peak positions and intensity. The sign + (−) means that peak positions are shifted to higher (lower) energy sides or that peak intensity becomes larger (smaller) by increasing the corresponding parameter, whereas zero indicates that the peak positions or peak intensity are not sensitive to the parameter.

Parameter	\bar{W}	δW	
	Position	Position	Intensity
F^0	+	+	+
F^2	0	0	+
G^1	−	−	+
G^3	−	−	+

In addition, F^0 uniformly shifts the eigenvalues of \bar{H}_{2p} . Because of the uniform shift, the results with $F^0 = 4.0$ eV in Fig. 9 are horizontally shifted for comparison. Figure 9 shows that the intensity of δW is approximately proportional to the square of F^0 because δW is the second-order perturbation with respect to V_{pd} , as shown in Eq. (50). The qualitative dependence on F^1 and G^1 is summarized in Table I.

D. Emission angle dependence

In the above calculations, the emission angle β with respect to the magnetization direction was set to the experimental setup value ($\beta = 60^\circ$). Here, we discuss the dependence of the XMCPE intensity on β . Figure 10 shows the β dependence of the calculated XMCPE spectra by the total W . The parameters except for β are the same as in Fig. 5. In the upper and middle panels of Fig. 10, the peak shapes and intensity do not change substantially. On the other hand, in the lower panel, the difference intensity at each peak position gives a cosinusoidal curve as a function of β . This indicates that measurement of the β dependence can determine magnetization directions in bulk. Theoretically, the angular dependence arises from the dipole transition matrix $w^{2p,1s}$ (see Appendix B). In \bar{H}_{2p} in Eq. (41), the $2p$ - $3d$ interaction is much smaller than the $2p$ spin-orbit interaction, and can be considered as a perturbation. Indeed, the four energy levels appearing in the \bar{W} spectra in Fig. 7 correspond well to $2p_{3/2}$ eigenvalues of h_{2p} under an effective external magnetic field causing Zeeman splitting. Hence, the unitary matrix element u_ζ^a is approximately the Clebsch-Gordan coefficient:

$$u_\zeta^a \approx \langle 1, m_\zeta; \frac{1}{2}, \sigma_\zeta | j_a, \mu_a \rangle, \quad (56)$$

where j_a and μ_a correspond to the total angular momentum and its projection quantum number of the a state, respectively. By combining $w^{2p,1s}$ and u_ζ^a , the following difference of coefficients between the positive and negative helicities shows a cosinusoidal dependence:

$$w_{a,\sigma}(\lambda) \equiv \sum_\zeta w_{\zeta,\sigma}^{2p,1s}(\Lambda_\lambda) u_\zeta^a \propto \sum_m \left\langle 1, m; \frac{1}{2}, \sigma \left| j_a, \mu_a \right. \right\rangle d_{m,\lambda}^{(1)}(\beta), \quad (57)$$

$$\sum_{\lambda=\pm} \sum_\sigma \text{sgn}(\lambda) |w_{a,\sigma}(\lambda)|^2 \propto \cos \beta, \quad (58)$$

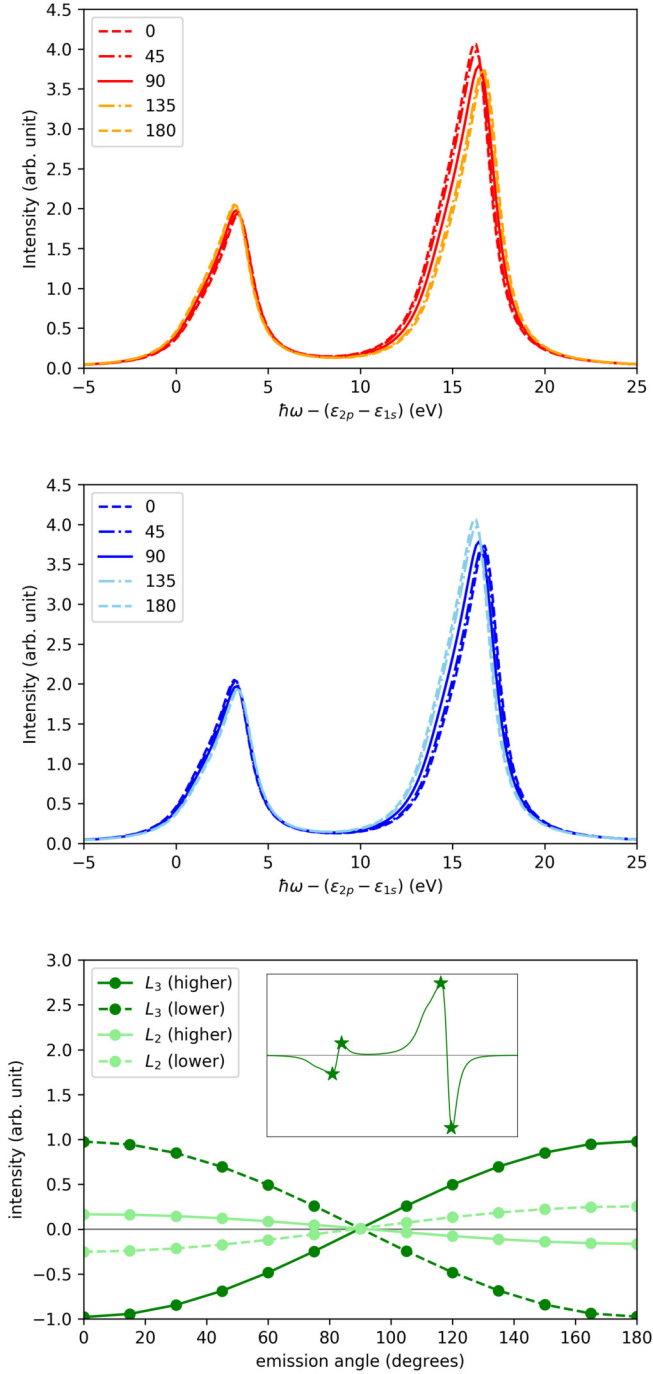


FIG. 10. Calculated right (upper panel) and left (middle panel) circular polarization terms using total W with various emission angles with respect to the magnetization direction. The lower panel shows the angular dependence of the calculated difference spectra at each peak position shown in the inset. The inset shows the calculated difference spectrum with an emission angle of 0° . The calculation parameters except for the emission angle are the same as those used in Fig. 5. The horizontal gray solid line indicates the zero value.

where $d(\beta)$ is the orthogonal Wigner's small d matrix with the angle β (see Appendix B). Difference spectra in XMCPe can

be given by

$$\begin{aligned} \Delta W &= \sum_{\lambda=\pm} \text{sgn}(\lambda) W_\lambda \\ &= \sum_{a,a'} \left(\sum_{\lambda=\pm} \sum_{\sigma} \text{sgn}(\lambda) w_{a,\sigma}(\lambda) (w_{a',\sigma}(\lambda))^* \right) I_{a,a'}, \end{aligned} \quad (59)$$

where the integral $I_{a,a'}$ corresponds to the integral in Eq. (38). When $I_{a,a'}$ is diagonal, the difference ΔW has a cosinusoidal dependence. Since $\bar{G}_a^{+,2p}$ defined in Eq. (44) is diagonal, the difference of the \bar{W} terms shows a cosinusoidal dependence. In addition, $\delta G_{a,a'}^{+,2p}$ defined in Eq. (50) is also diagonal according to our numerical calculations (results not shown). Therefore, ΔW exhibits cosinusoidal dependence, as shown in Fig. 10.

IV. CONCLUSION

We developed a theoretical method to calculate $K\alpha$ XM-CPE spectra for $3d$ -TM itinerant ferromagnets by using Keldysh Green's functions. We used our method to calculate the spectra of metallic iron. Reasonable agreement between the calculated and experimental results suggests that our theoretical framework is suitable for analyzing this new spectroscopic measurement. The itinerant $3d$ electron excitations yield additional peaks with lifetime broadening, which make the peak shapes of the total spectra asymmetric, consistent with the experimental spectra. The additional peaks possess the continuum nature reflecting the broadness of the d bands. We showed that the difference intensity should have a cosinusoidal dependence on the emission angle. The cosinusoidal dependence can be used to identify the magnetization directions inside bulk ferromagnets. Although we demonstrated the application of our theoretical framework to a simple TM, our approach can be extended easily to itinerant magnetic systems including several atoms in a unit cell.

ACKNOWLEDGMENT

This work was supported by the as follows JSPS Grant-in-Aid for Scientific Research (B) Grant No. 19H04405 and QST President's Strategic Grant (Exploratory Research).

APPENDIX A

In this Appendix, we briefly explain the mean-field approximation of H_{band} in Eq. (10). The number and the spin moment operators, n and \mathbf{m} , are defined as

$$n_{i,\mu,\sigma} = c_{i,\mu,\sigma}^\dagger c_{i,\mu,\sigma}, \quad (A1)$$

$$\mathbf{m}_{i,\mu} = \sum_{\sigma,\sigma'} c_{i,\mu,\sigma}^\dagger \vec{\sigma}_{\sigma\sigma'} c_{i,\mu,\sigma'}, \quad (A2)$$

where $\vec{\sigma}$ is the Pauli matrices. The Fourier transforms of those operators are

$$n_{\mathbf{q},\mu} = \frac{1}{N} \sum_{\mathbf{k},\sigma} c_{\mathbf{k},\mu,\sigma}^\dagger c_{\mathbf{k}+\mathbf{q},\mu,\sigma}, \quad (A3)$$

$$\mathbf{m}_{\mathbf{q},\mu} = \frac{1}{N} \sum_{\mathbf{k},\sigma,\sigma'} c_{\mathbf{k},\mu,\sigma}^\dagger \vec{\sigma}_{\sigma\sigma'} c_{\mathbf{k}+\mathbf{q},\mu,\sigma'}. \quad (A4)$$

By using the operators, the MF band Hamiltonian \bar{H}_{band} is given by

$$\bar{H}_{\text{band}} = h_{\text{TB}} + \bar{H}'_{\text{band}}, \quad (\text{A5})$$

$$\begin{aligned} \bar{H}'_{\text{band}}/N = & \sum_{\mathbf{q}, \mu} \left[\frac{U}{2} \langle n_{\mathbf{q}, \mu} \rangle^* + \left(U' - \frac{J}{2} \right) \sum_{\mu' (\neq \mu)} \langle n_{\mathbf{q}, \mu'} \rangle^* \right] n_{\mathbf{q}, \mu} \\ & - \sum_{\mathbf{q}, \mu} \left[\frac{U}{2} \langle \mathbf{m}_{\mathbf{q}, \mu} \rangle^* + \frac{J}{2} \sum_{\mu' (\neq \mu)} \langle \mathbf{m}_{\mathbf{q}, \mu'} \rangle^* \right] \cdot \mathbf{m}_{\mathbf{q}, \mu} \\ & + \bar{\varepsilon}, \end{aligned} \quad (\text{A6})$$

where $\bar{\varepsilon}$ just shifts the total energy. Since we assume a ferromagnetic phase without charge and spin fluctuations, the mean values of n and \mathbf{m} are given by

$$\langle n_{\mathbf{q}, \mu} \rangle \approx \langle n_{0, \mu} \rangle \delta_{\mathbf{q}, \mathbf{0}} \equiv \bar{n}_{\mu} \delta_{\mathbf{q}, \mathbf{0}}, \quad (\text{A7})$$

$$\langle \mathbf{m}_{\mathbf{q}, \mu} \rangle \approx \langle \mathbf{m}_{0, \mu} \rangle \delta_{\mathbf{q}, \mathbf{0}} \equiv (0, 0, \bar{m}_{\mu}) \delta_{\mathbf{q}, \mathbf{0}}, \quad (\text{A8})$$

where the spin polarization direction is assumed to be parallel to the z axis. The mean values \bar{n} and \bar{m} are averaged by the number of unit cells. By using the mean values, \bar{H}'_{band} is reduced to

$$\begin{aligned} \bar{H}'_{\text{band}} \approx & \sum_{\mathbf{k}, \mu, \sigma} \left[\frac{U}{2} (\bar{n}_{\mu} - \text{sgn}(\sigma) \bar{m}_{\mu}) \right. \\ & + \sum_{\mu' (\neq \mu)} \left(\left(U' - \frac{J}{2} \right) \bar{n}_{\mu'} - \text{sgn}(\sigma) \frac{J}{2} \bar{m}_{\mu'} \right) \left. \right] n_{\mathbf{k}, \mu, \sigma} \\ & + \bar{E}. \end{aligned} \quad (\text{A9})$$

Because the tight-binding Hamiltonian h_{TB} can have off-diagonal matrix elements, \bar{H}_{band} is diagonalized with respect to the band index γ which differs from the orbital index μ .

$$\begin{aligned} \bar{H}_{\text{band}} & \approx h_{\text{TB}} + \bar{H}'_{\text{band}} - \bar{H}_{\text{band}}^{\text{TB}} \\ & = \sum_{\mathbf{k}, \gamma, \sigma} E_{\mathbf{k}\gamma\sigma} c_{\mathbf{k}, \gamma, \sigma}^{\dagger} c_{\mathbf{k}, \gamma, \sigma}. \end{aligned} \quad (\text{A10})$$

Here, the double counting correction $\bar{H}_{\text{band}}^{\text{TB}}$ is \bar{H}'_{band} with the mean values of electron number and spin polarization obtained by solving only h_{TB} .

APPENDIX B

In this Appendix, we explain details of the dipole transition matrix w appearing in Eq. (5). First, we note the following relation,

$$[x, h_e] = \left[x, \frac{p^2}{2} + v_{ee}(\mathbf{r}) \right] = ip_x, \quad (\text{B1})$$

where h_e is the Hamiltonian including the electron-electron interaction v_{ee} . When a photon wave vector is parallel to the z direction, which is parallel to the quantization axis,

$$\hat{\varepsilon}_{\pm} \cdot \mathbf{p} = \mp \frac{1}{\sqrt{2}} (p_x \pm ip_y) = \mp \frac{1}{\sqrt{2}} \frac{1}{i} ([x, h_e] \pm i[y, h_e]). \quad (\text{B2})$$

Finally, the matrix element in w with circular polarization can be represented by spherical harmonics.

$$\begin{aligned} \langle n | \hat{\varepsilon}_{\pm} \cdot \mathbf{p} | n' \rangle & \propto \mp (E_{n'} - E_n) \langle n | (x \pm iy) | n' \rangle \\ & \propto (E_{n'} - E_n) \langle n | r Y_{1\pm 1}(\hat{\mathbf{r}}) | n' \rangle. \end{aligned} \quad (\text{B3})$$

Here, n and n' indicate each eigenstate of h_e , and E_n and $E_{n'}$ are their eigenvalues, respectively.

In general cases where the photon wave vector is tilted by β from the z axis, the spherical harmonic $Y_{lm}(\hat{\mathbf{r}})$ in Eq. (B3) is replaced by $Y_{lm}(\hat{\mathbf{r}}_{\beta})$ defined as

$$Y_{lm}(\hat{\mathbf{r}}) \rightarrow Y_{lm}(\hat{\mathbf{r}}_{\beta}) \equiv \sum_{m'} Y_{lm'}(\hat{\mathbf{r}}) d_{m'm}^{(l)}(\beta), \quad (\text{B4})$$

where $d_{m'm}^{(l)}(\beta)$ is an element of the orthogonal Wigner's small d matrix. For the dipole transition,

$$Y_{1\pm 1}(\hat{\mathbf{r}}_{\beta}) = \frac{1 \pm \cos \beta}{2} Y_{11}(\hat{\mathbf{r}}) \pm \frac{\sin \beta}{\sqrt{2}} Y_{10}(\hat{\mathbf{r}}) + \frac{1 \mp \cos \beta}{2} Y_{1-1}(\hat{\mathbf{r}}). \quad (\text{B5})$$

This provides the β dependence of XMCPE spectra.

Here, we show that the dipole transition matrices with either $1s$ or $2p$ core orbitals do not depend on the crystal momenta. The electronic Hamiltonian h_e corresponds to H_e defined in Eq. (6). For the matrix with the $1s$ and \tilde{p} states,

$$\begin{aligned} w_{\tilde{\mathbf{K}}\tilde{\sigma}, \mathbf{k}_1\sigma_1}^{\tilde{p}, 1s}(\Lambda_i) & \propto \frac{\varepsilon_{1s} - \varepsilon_{\tilde{\mathbf{K}}}}{\sqrt{\varepsilon_i}} \langle \psi_{\tilde{\mathbf{K}}\tilde{\sigma}}^{\tilde{p}} | r Y_{1\lambda_i}(\hat{\mathbf{r}}) | \psi_{\mathbf{k}_1\sigma_1}^{1s} \rangle \\ & \propto \frac{\varepsilon_{1s} - \varepsilon_{\tilde{\mathbf{K}}}}{\sqrt{\varepsilon_i}} \frac{1}{\sqrt{N}} \\ & \quad \times \sum_{i_1} e^{i\mathbf{k}_1 \cdot \mathbf{R}_{i_1}} \langle \psi_{\tilde{\mathbf{K}}\tilde{\sigma}}^{\tilde{p}} | r Y_{1\lambda_i}(\hat{\mathbf{r}}) | \psi_{i_1\sigma_1}^{1s} \rangle, \end{aligned} \quad (\text{B6})$$

$$\langle \mathbf{r} | \psi_{\tilde{\mathbf{K}}\tilde{\sigma}}^{\tilde{p}} \rangle = \frac{1}{\sqrt{\Omega}} e^{i\tilde{\mathbf{K}} \cdot \mathbf{r}} |\tilde{\sigma}\rangle, \quad (\text{B7})$$

$$\langle \mathbf{r} | \psi_{i_1\sigma_1}^{1s} \rangle = \psi_{1s}(r_{i_1}) Y_{00} | \sigma_1 \rangle \quad (r_{i_1} \equiv |\mathbf{r} - \mathbf{R}_{i_1}|). \quad (\text{B8})$$

Ω is the volume of the first Brillouin zone and \mathbf{R}_{i_1} is the position vector of the unit cell i_1 . A plane wave can be represented by the spherical harmonics and the spherical Bessel function $j_l(x)$ by using Bauer's formula:

$$e^{i\tilde{\mathbf{K}} \cdot \mathbf{r}} = 4\pi \sum_L i^L j_L(\tilde{\mathbf{K}}r) Y_L(\hat{\mathbf{r}}) Y_L^*(\hat{\tilde{\mathbf{K}}}). \quad (\text{B9})$$

Because of the translational symmetry of plane waves, the matrix elements do not depend on the unit-cell index:

$$\begin{aligned} & \langle \psi_{\tilde{\mathbf{K}}\tilde{\sigma}}^{\tilde{p}} | r Y_{1\lambda_i}(\hat{\mathbf{r}}) | \psi_{i_1\sigma_1}^{1s} \rangle \\ & = i \sqrt{\frac{4\pi}{\Omega}} \left(\int dr r^3 j_1(\tilde{\mathbf{K}}r) \psi_{1s}(r) \right) Y_{1\lambda_i}^*(-\hat{\tilde{\mathbf{K}}}) \delta_{\tilde{\sigma}, \sigma_1} \\ & \equiv I(\tilde{\mathbf{K}}) \delta_{\tilde{\sigma}, \sigma_1}. \end{aligned} \quad (\text{B10})$$

By using the relation $\sum_{i_1} e^{i\mathbf{k}_1 \cdot \mathbf{R}_{i_1}} = N \delta_{\mathbf{k}_1, \mathbf{0}}$,

$$w_{\tilde{\mathbf{K}}\tilde{\sigma}, \mathbf{k}_1\sigma_1}^{\tilde{p}, 1s}(\Lambda_i) \propto \frac{\varepsilon_{1s} - \varepsilon_{\tilde{\mathbf{K}}}}{\sqrt{\varepsilon_i}} I(\tilde{\mathbf{K}}) \delta_{\mathbf{k}_1, \mathbf{0}} \delta_{\tilde{\sigma}, \sigma_1}. \quad (\text{B11})$$

The dipole integral $I(\tilde{\mathbf{K}})$ slowly changes when $\tilde{\mathbf{K}}$ is sufficiently large. In the present XMCPE measurement, because

Λ_i is fixed and the deviation of $\omega_{\tilde{K}}$ is small compared with $\sqrt{\omega_i}$, $w^{\tilde{p},1s}$ can be regarded as a constant.

For the matrix with $1s$ and $2p$ states, we adopt the diagonal $1s$ Hamiltonian h_{1s} and the MF $2p$ Hamiltonian \bar{H}_{2p} . As a result,

$$w_{\mathbf{k}\zeta, \mathbf{k}_1\sigma_1}^{2p,1s}(\Lambda_f) \propto \sum_a \sum_{\zeta'} \frac{\varepsilon_{1s} - E_a}{\sqrt{\varepsilon_f}} (u_{\zeta}^a)^* (u_{\zeta'}^a)^* \times \langle \psi_{\mathbf{k}\zeta'}^{2p} | rY_{1\lambda_f}(\hat{\mathbf{r}}_{\beta}) | \psi_{\mathbf{k}_1\sigma_1}^{1s} \rangle, \quad (\text{B12})$$

$$\begin{aligned} & \langle \psi_{\mathbf{k}\zeta'}^{2p} | rY_{1\lambda_f}(\hat{\mathbf{r}}) | \psi_{\mathbf{k}_1\sigma_1}^{1s} \rangle \\ &= \frac{1}{N} \sum_{i,i_1} e^{-i\mathbf{k}\cdot\mathbf{R}_i} e^{i\mathbf{k}_1\cdot\mathbf{R}_{i_1}} \langle \psi_{i\zeta'}^{2p} | rY_{1\lambda_f}(\hat{\mathbf{r}}_{\beta}) | \psi_{i_1\sigma_1}^{1s} \rangle, \quad (\text{B13}) \end{aligned}$$

where the index a indicates each eigenstate of \bar{H}_{2p} . Since the $1s$ or $2p$ core orbitals are well localized within a unit cell or an atomic site,

$$\begin{aligned} \langle \psi_{i\zeta'}^{2p} | rY_{1\lambda_f}(\hat{\mathbf{r}}_{\beta}) | \psi_{i_1\sigma_1}^{1s} \rangle &= \langle \psi_{i\zeta'}^{2p} | rY_{1\lambda_f}(\hat{\mathbf{r}}_{\beta}) | \psi_{i_1\sigma_1}^{1s} \rangle \delta_{\sigma_a, \sigma_1} \delta_{i, i_1} \\ &= I_{2p}^{1s} d_{m_{\zeta'}, \lambda_f}^{(1)}(\beta) \delta_{\sigma_{\zeta'}, \sigma_1} \delta_{i, i_1}, \quad (\text{B14}) \end{aligned}$$

$$I_{2p}^{1s} \equiv \int dr r^3 \psi_{2p}^*(r) \psi_{1s}(r). \quad (\text{B15})$$

Finally, by using the relation $\sum_i e^{i(\mathbf{k}_1 - \mathbf{k})\cdot\mathbf{R}_i} = N\delta_{\mathbf{k}, \mathbf{k}_1}$,

$$\begin{aligned} w_{\mathbf{k}\zeta, \mathbf{k}_1\sigma_1}^{2p,1s}(\Lambda_f) &\propto \sum_a \sum_{\zeta'} \frac{\varepsilon_{1s} - E_a}{\sqrt{\varepsilon_f}} (u_{\zeta}^a)^* (u_{\zeta'}^a)^* \\ &\quad \times d_{m_{\zeta'}, \lambda_f}^{(1)}(\beta) \delta_{\sigma_{\zeta'}, \sigma_1} \delta_{\mathbf{k}, \mathbf{k}_1} \\ &\equiv w_{\mathbf{k}\zeta, \sigma_1}^{2p,1s}(\Lambda_f) \delta_{\mathbf{k}, \mathbf{k}_1}. \quad (\text{B16}) \end{aligned}$$

Although $w_{\mathbf{k}\zeta, \sigma_1}^{2p,1s}$ does not depend on \mathbf{k} , we keep the index \mathbf{k} explicitly for clarity. In \bar{H}_{2p} in Eq. (41), the $2p$ - $3d$ interaction can be considered as a perturbation. In particular, the F^0 term shifts whole eigenvalues, and the G^1 term causes exchange splittings in $2p$ sublevels. The splittings are few electronvolts in size and are negligibly smaller than the emission energy ω_f or the energy difference $|\varepsilon_{1s} - \varepsilon_{2p}|$, and thus we have

$$w_{\mathbf{k}\zeta, \sigma_1}^{2p,1s}(\Lambda_f) \approx \frac{\varepsilon_{1s} - \bar{E}_{2p}}{\sqrt{\varepsilon_f}} d_{m_{\zeta'}, \lambda_f}^{(1)}(\beta), \quad (\text{B17})$$

where \bar{E}_{2p} is the average of the eigenvalues of \bar{H}_{2p} .

-
- [1] G. Schütz, W. Wagner, W. Wilhelm, P. Kienle, R. Zeller, R. Frahm, and G. Materlik, Absorption of Circularly Polarized X Rays in Iron, *Phys. Rev. Lett.* **58**, 737 (1987).
- [2] C. T. Chen, Y. U. Idzerda, H.-J. Lin, N. V. Smith, G. Meigs, E. Chaban, G. H. Ho, E. Pellegrin, and F. Sette, Experimental Confirmation of the X-Ray Magnetic Circular Dichroism Sum Rules for Iron and Cobalt, *Phys. Rev. Lett.* **75**, 152 (1995).
- [3] O. Mathon, F. Baudelet, J.-P. Itié, S. Pasternak, A. Polian, and S. Pascarelli, XMCD under pressure at the Fe K edge on the energy-dispersive beamline of the ESRF, *J. Synchrotron Rad.* **11**, 423 (2004).
- [4] J. Stöhr and H. C. Siegmann, *Magnetism From Fundamentals to Nanoscale Dynamics* (Springer-Verlag, Berlin, Heidelberg, 2006).
- [5] E. Beaupaire, H. Bulou, F. Scheurer, and J. P. Kappler, editors, *Magnetism: A Synchrotron Radiation Approach* (Springer-Verlag, Berlin, Heidelberg, 2006).
- [6] P. Strange, P. J. Durham, and B. L. Gyorffy, Dichroic X-Ray Fluorescence, *Phys. Rev. Lett.* **67**, 3590 (1991).
- [7] C. F. Hague, J.-M. Mariot, P. Strange, P. J. Durham, and B. L. Gyorffy, Observation of magnetic circular dichroism in Fe $L_{2,3}$ x-ray fluorescence spectra, *Phys. Rev. B* **48**, 3560 (1993).
- [8] M. H. Krisch, F. Sette, U. Bergmann, C. Masciovecchio, R. Verbeni, J. Goulon, W. Caliebe, and C. C. Kao, Observation of magnetic circular dichroism in resonant inelastic x-ray scattering at the L_3 edge of gadolinium metal, *Phys. Rev. B* **54**, R12673 (1996).
- [9] F. M. F. de Groot, M. Nakazawa, A. Kotani, M. H. Krisch, and F. Sette, Theoretical analysis of the magnetic circular dichroism in the $2p3d$ and $2p4d$ x-ray emission of Gd, *Phys. Rev. B* **56**, 7285 (1997).
- [10] L.-C. Duda, J. Stöhr, D. C. Mancini, A. Nilsson, N. Wassdahl, J. Nordgren, and M. G. Samant, Magnetic dichroism in $L_{2,3}$ emission of Fe, Co, and Ni following energy-dependent excitation with circularly polarized x rays, *Phys. Rev. B* **50**, 16758 (1994).
- [11] C.-F. Hague, J.-M. Mariot, G. Y. Guo, K. Hricovini, and G. Krill, Coster-Kronig contributions to magnetic circular dichroism in the $L_{2,3}$ x-ray fluorescence of iron, *Phys. Rev. B* **51**, 1370 (1995).
- [12] T. Iwazumi, K. Kobayashi, S. Kishimoto, T. Nakamura, S. Nanao, D. Ohsawa, R. Katano, and Y. Isozumi, Magnetic resonance effect in x-ray resonant Raman scattering, *Phys. Rev. B* **56**, R14267 (1997).
- [13] L. Braicovich, G. van der Laan, G. Ghiringhelli, A. Tagliaferri, M. A. van Veenendaal, N. B. Brookes, M. M. Chervinskii, C. Dallera, B. DeMichelis, and H. A. Dürr, Dyaloshinskii-Moriya Interaction in α -Fe $_2$ O $_3$ Measured by Magnetic Circular Dichroism in Resonant Inelastic Soft X-Ray Scattering, *Phys. Rev. Lett.* **82**, 1566 (1999).
- [14] M. Sikora, A. Juhin, T.-C. Weng, P. Sainctavit, C. Detlefs, F. de Groot, and P. Glatzel, Strong K -Edge Magnetic Circular Dichroism Observed in Photon-in-Photon-out Spectroscopy, *Phys. Rev. Lett.* **105**, 037202 (2010).
- [15] M. Sikora, A. Juhin, G. Simon, M. Zajac, K. Biernacka, C. Kapusta, L. Murellon, M. R. Ibarra, and P. Glatzel, $1s2p$ resonant inelastic x-ray scattering-magnetic circular dichroism: A sensitive probe of $3d$ magnetic moments using hard x-ray photons, *J. Appl. Phys.* **111**, 07E301 (2012).
- [16] J. Miyawaki, S. Suga, H. Fujiwara, M. Urasaki, H. Ikeno, H. Niwa, H. Kiuchi, and Y. Harada, Dyaloshinskii-Moriya interaction in α -Fe $_2$ O $_3$ measured by magnetic circular dichroism in

- resonant inelastic soft x-ray scattering, *Phys. Rev. B* **96**, 214420 (2017).
- [17] P. Zimmermann, N. Bouldi, M. O. J. Y. Hunault, M. Sikora, J. M. Ablett, J.-P. Rueff, B. Lebert, P. Sainctavit, F. M. F. de Groot, and A. Juhin, 1s2p resonant inelastic x-ray scattering magnetic circular dichroism as a probe for the local and non-local orbitals in CrO₂, *J. Electron Spectrosc. Relat. Phenom.* **222**, 74 (2018).
- [18] T. Inami, Magnetic Circular Dichroism in X-Ray Emission from Ferromagnets, *Phys. Rev. Lett.* **119**, 137203 (2017).
- [19] X. Wang, F. M. F. de Groot, and S. P. Cramer, Spin-polarized x-ray emission of 3d transition-metal ions: A comparison via $K\alpha$ and $K\beta$ detection, *Phys. Rev. B* **56**, 4553 (1997).
- [20] H. Ebert, Theory of circularly polarized x-ray absorption by ferromagnetic Fe, *J. Appl. Phys.* **63**, 3055 (1988).
- [21] J.-I. Igarashi and K. Hirai, Magnetic circular dichroism at the K edge of nickel and iron, *Phys. Rev. B* **50**, 17820 (1994).
- [22] J.-I. Igarashi and K. Hirai, Orbital moment and magnetic circular dichroism at the K edge in ferromagnetic cobalt, *Phys. Rev. B* **53**, 6442 (1996).
- [23] C. Brouder, M. Alouani, and K. H. Bennemann, Multiple-scattering theory of x-ray magnetic circular dichroism: Implementation and results for the iron K edge, *Phys. Rev. B* **54**, 7334 (1996).
- [24] H. Ebert, Magneto-optical effects in transition metal systems, *Rep. Prog. Phys.* **59**, 1665 (1996).
- [25] J. Henk, A. M. N. Niklasson, and B. Johansson, Multiple-scattering theoretical approach to magnetic dichroism and spin polarization in angle-resolved core-level photoemission, *Phys. Rev. B* **59**, 13986 (1999).
- [26] N. Bouldi, N. J. Vollmers, C. G. Delpy-Laplanche, Y. Joly, A. Juhin, P. Sainctavit, C. Brouder, M. Calandra, L. Paulatto, F. Mauri, and U. Gerstmann, X-ray magnetic and natural circular dichroism from first principles: Calculation of K - and L_1 -edge spectra, *Phys. Rev. B* **96**, 085123 (2017).
- [27] H. Ebert, L. Baumgarten, C. M. Schneider, and J. Kirschner, Polarization dependence of the 2p-core-level photoemission spectra of Fe, *Phys. Rev. B* **44**, 4406 (1991).
- [28] A. Georges, G. Kotliar, W. Krauth, and M. J. Rozenberg, Dynamical mean-field theory of strongly correlated fermion systems and the limit of infinite dimensions, *Rev. Mod. Phys.* **68**, 13 (1996).
- [29] J. Braun, J. Minár, H. Ebert, M. I. Katsnelson, and A. I. Lichtenstein, Spectral Function of Ferromagnetic 3d Metals: A Self-Consistent LSDA + DMFT Approach Combined with the One-Step Model of Photoemission, *Phys. Rev. Lett.* **97**, 227601 (2006).
- [30] O. Šípr, J. Minár, A. Scherz, H. Wende, and H. Ebert, Many-body effects in x-ray absorption and magnetic circular dichroism spectra within the LSDA+DMFT framework, *Phys. Rev. B* **84**, 115102 (2011).
- [31] E. L. Shirley, Bethe-Salpeter treatment of x-ray absorption including core-hole multiplet effects, *J. Electron Spectrosc. Relat. Phenom.* **144-147**, 1187 (2005).
- [32] J. Vinson and J. J. Rehr, *Ab initio* Bethe-Salpeter calculations of the x-ray absorption spectra of transition metals at the L-shell edges, *Phys. Rev. B* **86**, 195135 (2012).
- [33] J. C. Slater, The theory of complex spectra, *Phys. Rev.* **34**, 1293 (1929).
- [34] E. U. Condon, The theory of complex spectra, *Phys. Rev.* **36**, 1121 (1930).
- [35] E. U. Condon and G. H. Shortley, *The Theory of Atomic Spectra* (Cambridge University Press, Cambridge, 1959).
- [36] J. Kanamori, Electron correlation and ferromagnetism of transition metals, *Prog. Theor. Phys.* **30**, 275 (1963).
- [37] H. Mizuta and A. Kotani, Theory of spin-polarized auger electrons from ferromagnetic materials, *J. Phys. Soc. Jpn.* **54**, 4452 (1985).
- [38] V. I. Anisimov and O. Gunnarsson, Density-functional calculation of effective Coulomb interactions in metals, *Phys. Rev. B* **43**, 7570 (1991).
- [39] P. Nozières and E. Abrahams, Threshold singularities of the x-ray Raman scattering in metals, *Phys. Rev. B* **10**, 3099 (1974).
- [40] L. V. Keldysh, Diagram technique for nonequilibrium processes, *Sov. Phys. JETP* **20**, 1018 (1965).
- [41] P. Blaha, K. Schwarz, G. Madsen, D. Kvasnicka, and J. Luitz, *WIEN2k, An Augmented Plane Wave Plus Local Orbitals Program for Calculating Crystal Properties*, 2nd ed. (Vienna University of Technology, Vienna, 2001).
- [42] J. P. Perdew, K. Burke, and M. Ernzerhof, Generalized Gradient Approximation Made Simple, *Phys. Rev. Lett.* **77**, 3865 (1996).
- [43] A. A. Mostofi, J. R. Yates, G. Pizzi, Y. S. Lee, I. Souza, D. Vanderbilt, and N. Marzari, An updated version of Wannier90: A tool for obtaining maximally-localised Wannier functions, *Comput. Phys. Commun.* **185**, 2309 (2014).
- [44] K. Sugawara and T. Inami (unpublished).
- [45] R. D. Cowan, *The Theory of Atomic Structure and Spectra* (University of California Press, Berkeley, 1981).
- [46] M. O. Krause and J. H. Oliver, Natural widths of atomic K and L levels, $K\alpha$ x-ray lines and several KLL auger lines, *J. Phys. Chem. Ref. Data* **8**, 329 (1979).
- [47] P. S. Miedema, F. Borgatti, F. Offi, G. Panaccione, and F. M. F. de Groot, Iron 1s x-ray photoemission of Fe₂O₃, *J. Electron Spectrosc. Relat. Phenomena* **203**, 8 (2015).